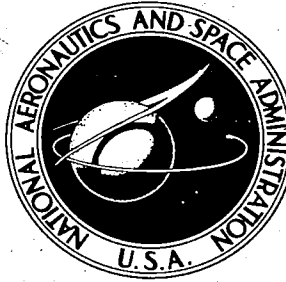



**NASA TECHNICAL
REPORT**



NASA TR R-181

C. 2

LOAN COPY: 
AFWL (WPA) 1054941
KIRTLAND AFB

TECH LIBRARY KAFB, NM

**EFFECT OF UNIFORM EXTERNAL PRESSURE
AND OBLIQUE INCIDENCE OF THE
SOLAR WIND ON THE TERMINAL SHAPE
OF THE GEOMAGNETIC FIELD**

by John R. Spreiter and Audrey L. Summers

Ames Research Center

Moffett Field, Calif.



0068081

EFFECT OF UNIFORM EXTERNAL PRESSURE AND OBLIQUE
INCIDENCE OF THE SOLAR WIND ON THE TERMINAL
SHAPE OF THE GEOMAGNETIC FIELD

By John R. Spreiter and Audrey L. Summers

Ames Research Center
Moffett Field, Calif.

NATIONAL AERONAUTICS AND SPACE ADMINISTRATION

For sale by the Office of Technical Services, Department of Commerce,
Washington, D.C. 20230 -- Price \$1.00

NATIONAL AERONAUTICS AND SPACE ADMINISTRATION

TECHNICAL REPORT R-181

EFFECT OF UNIFORM EXTERNAL PRESSURE AND OBLIQUE
INCIDENCE OF THE SOLAR WIND ON THE TERMINAL
SHAPE OF THE GEOMAGNETIC FIELD*

By John R. Spreiter and Audrey L. Summers

SUMMARY

Approximate solutions and numerical results are given for the coordinates of the boundary separating the geomagnetic field from the interplanetary plasma for a $\pm 35^\circ$ range of angles between the direction of the incident stream and the geomagnetic equatorial plane for a model that assumes the plasma pressure exerted on the boundary to be composed of two components. One is a dynamic pressure proportional to the normal component of the momentum of the particles of a steady uniform incident stream, as is customary in the usual formulation of the steady-state Chapman-Ferraro problem. The other is a static pressure considered to be constant over the entire boundary, including the shielded portions adjacent to dead-water regions on the downwind side of the earth and near the neutral points. Results are presented for the traces of the boundary in the meridian plane containing the sun-earth line and the dipole axis for a complete range of values for the ratio between the two pressure components. Corresponding results are also presented for the equatorial traces of the boundary for the case in which the dipole axis is normal to the sun-earth line. The principal qualitative feature of including the effect of a uniform external pressure is that the geomagnetic field terminates at a finite distance from the earth in the antisolar direction that is only a moderate multiple greater than in the solar direction for all but extremely small ratios of static to dynamic pressure. This result indicates that the asymmetry between the distances to the boundary of the geomagnetic field on the day and night sides of the earth may be greatly exaggerated by the results of the usual calculations in which the static pressure is disregarded.

INTRODUCTION

The present paper reports the results of an extension of the theoretical studies reported in references 1 through 4 of the form of the stationary cavity carved out of a neutral ionized corpuscular stream by the geomagnetic field. The

*Those results for normal incidence appeared previously in the Journal of Geophysical Research, vol. 68, no. 6, Mar. 15, 1963, pp. 1631-1642.

novel feature involved in this extension is the inclusion of the effect of a term to represent the static pressure of the interplanetary gas. This term is of considerable importance even when the static pressure is much less than the dynamic pressure of the stream because the closure of the boundary of the geomagnetic field on the night or shielded side of the earth depends entirely on the static pressure exerted by the more or less stationary wake. It is important to realize that this portion of the boundary of the geomagnetic field does not necessarily coincide with the boundary of the streaming interplanetary plasma, since the latter may trail off from the vicinity of the widest portion of the cavity much as in the more familiar case of separated free-streamline flow of a nonconducting fluid. A partial account of this investigation confined to the case in which the solar wind is normal to the dipole axis has been presented in reference 5. The present report is more complete, however, in that other relative orientations are included, and numerical tables of the coordinates of the boundary are presented in addition to plots for all cases.

The present study is also closely related to the investigations reported by Slutz (ref. 6) and by Midgley and Davis (ref. 7) in which the coordinates of the cavity are calculated for the case in which the interplanetary gas is stationary so that there exists a uniform static pressure, but no dynamic pressure. The latter analysis is superior to that presented herein for the same case, however, since it leads through application of numerical procedures to a solution that is essentially exact.

The present analysis, on the other hand, is based on the use of the approximation introduced and commented upon recently by Beard (ref. 1), Ferraro (ref. 8), and Davis and Beard (ref. 9). It is judged on the basis of previous experience that results obtained in this way display nearly all the essential features of the exact solution, although the coordinates of the boundary may be in error by a few percent one way or the other at various points. This statement is based on comparisons of exact and approximate solutions for the case of zero dynamic pressure given by Slutz (ref. 6) and by Midgley and Davis (ref. 7), and for the analogous problem in two-dimensions for the case of zero static pressure given by Hurley (ref. 10) and by Spreiter and Briggs (refs. 2 and 3).

It is considered in the present analysis, as in all those described in the references listed above, that the geomagnetic field in the vicinity of the earth can be represented by a three-dimensional dipole. As in the previous papers, the direction of the incident stream will be referred to for convenience as though it were coming directly from the sun. It should be understood, however, that the direction of the sun is actually immaterial in the analysis, and that only the direction of the uniform stream relative to the dipole axis is of significance.

FUNDAMENTAL CONCEPTS AND EQUATIONS

The fundamental concepts and equations of the present study have grown out of a long series of investigations by Chapman and Ferraro and others, recent summaries of which are given by Chapman (refs. 10 and 11) and Dungey (ref. 12). According to the model that has evolved from those investigations, the determination of the shape of the boundary of the geomagnetic field and the magnetic

field \vec{B} inside it requires the solution of the magnetic field equations $\text{div } \vec{B} = 0$ and $\text{curl } \vec{B} = 0$. (The principal symbols are defined in the appendix.) The total magnetic field \vec{B} is the sum of the permanent magnetic field \vec{B}_p and the induced magnetic field \vec{B}' due to the currents in the boundary. The total field thus depends on the shape of the boundary. The permanent magnetic field is represented by a three-dimensional dipole singularity at the origin (the center of the earth); thus \vec{B}_p is given by

$$\vec{B}_p = -(M_p/r^3)(\hat{l}_\theta \sin \theta + \hat{l}_r \cos \theta) \quad (1)$$

where the coordinate system is fixed with respect to the dipole axis as illustrated in figure 1, \hat{l}_θ and \hat{l}_r are unit vectors in the direction of increasing θ and r , and the magnetic moment of the dipole is given by $M_p = a^3 B_{p0}$ where a represents the radius of the earth and B_{p0} represents the intensity of the geomagnetic field at the magnetic equator. It is further required that the normal component of \vec{B} vanish at the boundary, and that the total (tangential) field at the boundary, B_s , have such a value that the magnetic pressure $B_s^2/8\pi$ balances the mechanical pressure of the incident particles. The latter condition is approximated in the present study by the relation

$$B_s^2/8\pi = 2mnv^2 \cos^2 \psi + p_0 = p_d \cos^2 \psi + p_0 \quad \text{for } \cos \psi \leq 0 \quad (2a)$$

for those portions of the boundary exposed to particles of the undisturbed stream, and by

$$B_s^2/8\pi = p_0 \quad \text{for } \cos \psi \geq 0 \quad (2b)$$

for the remainder of the boundary which is shielded from the direct impact of the particles of the undisturbed stream. The quantities p_d and p_0 are constants for any given example and are referred to hereinafter as the dynamic and static pressures. The boundary condition given by equation (2) has also been used by Slutz in a paper presented at the spring 1962 URSI meeting in Washington, D. C. The quantities m , n , and v are the mass, number density, and velocity of the protons of the solar stream, and ψ is the angle between the free-stream velocity vector and an outward normal to the surface. The quantities in the above equations are in electromagnetic units, and numerical values for a , B_{p0} , and m are 6.37×10^8 cm, 0.312 gauss, and 1.67×10^{-24} gm, respectively.

Beard (ref. 1) dropped the condition that the normal component of \vec{B} vanish at the boundary and replaced it with the approximate condition that $B_s = 2B_t$, where B_t is the tangential component of the geomagnetic dipole field \vec{B}_p at the boundary. The closely related approximation, suggested by Ferraro in reference 8 and earlier publications,

$$B_s = 2fB_t \quad (3)$$

where f is a constant, was used in references 2 through 5 and is employed in the present work.

The differential equation that defines, approximately, the shape of the boundary is obtained by substitution of equations (1) and (3) into equation (2).

It is

$$\begin{aligned}
& \frac{1}{\rho^6} \left[\left(\frac{1 + 3 \cos^2 \theta}{\rho^2 \sin^2 \theta} \right) \left(\frac{\partial \rho}{\partial \varphi} \right)^2 + \left(\sin \theta + \frac{2 \cos \theta}{\rho} \frac{\partial \rho}{\partial \theta} \right)^2 \right] \\
&= \frac{p_0}{p_d} \left[1 + \left(\frac{1}{\rho} \frac{\partial \rho}{\partial \theta} \right)^2 + \left(\frac{1}{\rho \sin \theta} \frac{\partial \rho}{\partial \varphi} \right)^2 \right] + \left[(\sin \varphi \sin \theta \cos \lambda - \cos \theta \sin \lambda) \right. \\
&\quad \left. - \frac{1}{\rho} \frac{\partial \rho}{\partial \theta} (\sin \varphi \cos \theta \cos \lambda + \sin \theta \sin \lambda) - \frac{\cos \varphi}{\rho \sin \theta} \frac{\partial \rho}{\partial \varphi} \cos \lambda \right]^2
\end{aligned} \tag{4a}$$

for $\cos \psi \leq 0$, and

$$\frac{1}{\rho^6} \left(\sin \theta + \frac{2 \cos \theta}{\rho} \frac{\partial \rho}{\partial \theta} \right)^2 = \frac{p_0}{p_d} \left[1 + \left(\frac{1}{\rho} \frac{\partial \rho}{\partial \theta} \right)^2 \right] \tag{4b}$$

for $\cos \psi \geq 0$, where $\partial \rho / \partial \varphi = 0$. In these expressions, λ represents the angle between the direction of the incident stream and geomagnetic equatorial plane as illustrated in figure 1, $\rho = r/r_0$, and r_0 is given by

$$r_0 = \left(\frac{4f^2 M_p^2}{16\pi m n v^2} \right)^{1/6} = a \left(\frac{4f^2 B_{p0}^2}{16\pi m n v^2} \right)^{1/6} = a \left(\frac{4f^2 B_{p0}^2}{8\pi p_d} \right)^{1/6} \tag{5}$$

The quantity r_0 is the geocentric distance along the sun-earth line to the boundary of the geomagnetic field for the special case in which $p_0 = 0$ and $\lambda = 0$. Representative values based on data from Mariner II (ref. 13) of $v = 5 \times 10^7$ cm/sec = 500 km/sec and $n = 2.5$ protons/cm³ lead to a value for r_0 of 9.5 earth radii for $f = 1$.

It should be observed that the left side of equation (4a) is as indicated by Davis and Beard in reference 9 and differs from that used previously by Beard (refs. 1 and 14) and by Spreiter and Briggs (refs. 2 and 3) as a result of the correction of an error in the evaluation of B_t in the approximate boundary condition indicated by equation (3). As noted by Davis and Beard, the error disappears when attention is confined to the meridian plane containing the sun-earth line; that is, $\varphi = \pm\pi/2$, and to the equatorial plane $\theta = \pi/2$ for the case in which the dipole axis is normal to the direction of the incident stream. Solutions given previously for these planes for the case $p_0 = 0$ are thus correct in spite of their derivation, but results for the coordinates of the remainder of the surface must be recalculated in order to be consistent with equation (3). In the present paper results are given for a wide variety of values for p_0/p_d but only for the traces of the boundary in the equatorial plane and in the meridian plane containing the sun-earth line. The results for the equatorial plane are confined, moreover, to the case in which the dipole axis is normal to the

direction of the incident stream, that is, $\lambda = 0$. The problem simplifies greatly for these planes because the partial differential equation given by equation (4a) reduces to an ordinary differential equation by reason of symmetry.

SOLUTION FOR THE EQUATORIAL PLANE, $\lambda = 0$

The determination of the trace of the boundary of the geomagnetic field in the equatorial plane for the case in which the dipole axis is normal to the direction of the incident stream requires consideration of the following equations obtained from equations (4a) and (4b) by equating λ to 0, θ to $\pi/2$, $\partial\rho/\partial\theta$ to 0, and by restricting attention to the interval $\pi/2 \leq \varphi \leq 3\pi/2$:

$$\frac{1}{\rho^6} = \frac{\left(\sin \varphi - \frac{\cos \varphi}{\rho} \frac{d\rho}{d\varphi}\right)^2}{1 + \left(\frac{1}{\rho} \frac{d\rho}{d\varphi}\right)^2} + \frac{p_0}{p_d} \quad \text{for } \cos \psi \leq 0 \quad (6a)$$

and

$$\frac{1}{\rho^6} = \frac{p_0}{p_d} \quad \text{for } \cos \psi \geq 0 \quad (6b)$$

It follows immediately that the shielded portion of the equatorial trace of the boundary is a segment of a circle of radius

$$\rho = (p_d/p_0)^{1/6} \quad (7)$$

The remaining portion of the equatorial trace is given by the solution of equation (6a), which reduces to the following upon solving for $d\rho/d\varphi$

$$\frac{d\rho}{d\varphi} = \rho \left\{ \frac{\rho^6 \sin \varphi \cos \varphi + \sqrt{\left[\rho^6 \left(1 + \frac{p_0}{p_d}\right) - 1\right] \left(1 - \rho^6 \frac{p_0}{p_d}\right)}}{\rho^6 \left(\cos^2 \varphi + \frac{p_0}{p_d}\right) - 1} \right\} \quad (8)$$

Thus, all integral curves representing real solutions are confined within the annular region defined by

$$\left(1 + \frac{p_0}{p_d}\right)^{-1/6} \leq \rho \leq \left(\frac{p_0}{p_d}\right)^{-1/6} \quad (9)$$

At the outer limiting circle, which also coincides with the trace of the shielded portion of the equatorial trace defined by equation (7), equation (8) reduces to

$$\frac{d\rho}{d\varphi} = \rho \tan \varphi \quad (10)$$

This result indicates that all integral curves of equation (8) are parallel to the incident stream at the point where they intersect the outer limiting circle. At the inner limiting circle, equation (8) reduces to

$$\frac{d\rho}{d\varphi} = -\rho \cot \varphi \quad (11)$$

which indicates all integral curves of equation (8) are normal to the direction of the incident stream at the point where they intersect the inner limiting circle.

These features of the solution of equation (8) are illustrated in the plot of the integral curves for the case $p_o/p_d = 1$ presented in figure 2. These and other integral curves shown herein have been determined numerically on an IBM 7090 electronic computer. Also indicated by dashed lines are the limiting circles defined by equation (9). The desired solution for the equatorial trace of the boundary of the exposed portion of the geomagnetic field for this case is thus defined by the integral curve that is tangent to the inner limiting circle at the point of intersection with the y axis. It has the property of being tangent to the outer limiting circle at the point of intersection with the x axis, and therefore joins smoothly to the circle of radius $(p_d/p_o)^{1/6}$ that represents the shielded portion of the boundary. The bounds on ρ indicated by equation (9) thus correspond physically to the minimum and maximum geocentric distances to the equatorial trace of the boundary of the geomagnetic field with the former occurring on the daytime side and the latter on the nighttime side of the earth.

Integral curves for p_o/p_d greater than unity are similar in all main features to those shown in figure 2. The principal difference is that the annular space within which the integral curves are confined becomes increasingly smaller as the radii of the inner and outer limiting circles approach a common value.

The results for p_o/p_d less than unity are somewhat different, however, since the integral curve of equation (8) that is tangent to the inner limiting circle at the point of intersection of the y axis does not extend to the outer limiting circle at the point of intersection with the x axis. These properties of the integral curves of equation (8) for the case $p_o/p_d = 0.01$ are illustrated in figure 3. The desired solution for the equatorial trace of the boundary of the geomagnetic field for this case is thus defined by the integral curve that extends from the point of intersection of the inner limiting circle and the y axis, together with the portion of the outer limiting circle necessary to close the boundary in the shielded region. It is anticipated that the corner indicated in the boundary would not be present in an exact solution, but results from the approximation introduced by the use of equation (3). Results calculated in this way for a wide range of values for p_o/p_d are shown graphically in figure 4 and listed in tabular form in table I.

SOLUTION FOR THE MERIDIAN PLANE CONTAINING THE SUN-EARTH LINE, $\lambda = 0$

The determination of the trace of the boundary of the geomagnetic field in the meridian plane containing the sun-earth line for the case in which the dipole axis is normal to the direction of the incident stream requires solution of equation (4) with λ equated to zero, φ to $\pm\pi/2$, and $\partial\rho/\partial\varphi$ to zero. Equation (4a) thus becomes

$$\frac{1}{\rho^6} \left(\sin \theta + \frac{2 \cos \theta}{\rho} \frac{d\rho}{d\theta} \right)^2 = \frac{p_0}{p_d} \left[1 + \left(\frac{1}{\rho} \frac{d\rho}{d\theta} \right)^2 \right] + \left(\sin \theta - \frac{\cos \theta}{\rho} \frac{d\rho}{d\theta} \right)^2 \quad (12)$$

and equation (4b) remains unchanged.

If the new quantity R defined by

$$R = \rho(p_0/p_d)^{1/6} \quad (13)$$

is introduced, equation (4b) can be written as follows after solving for $dR/d\theta$:

$$\frac{dR}{d\theta} = \frac{-2R \sin \theta \cos \theta \pm R^4 \sqrt{1 + 3 \cos^2 \theta - R^6}}{4 \cos^2 \theta - R^6} \quad (14)$$

Thus, all integral curves representing real solutions are confined to the interior of the region bounded by the limiting line defined by

$$R = (1 + 3 \cos^2 \theta)^{1/6} \quad (15)$$

Plots of the integral curves of equation (14) with both the upper (plus) and lower (minus) sign are shown in figure 5. The limiting curve indicated by equation (15) with the equal sign is indicated by the dashed line. Of all the integral curves, only one member of the family shown in figure 5(a) crosses the y axis at a finite distance from the dipole at the origin and at a right angle to the direction of the incident stream. This curve, moreover, crosses the y axis at a geocentric distance $R = 1$, and thereby intersects the equatorial plane at the distance given by equation (7). It, therefore, satisfies all the conditions required for the solution representing the shielded part of the boundary of the geomagnetic field on the nighttime side of the earth.

The entire curve also represents the shape of the boundary of the geomagnetic field in the limiting case in which the interplanetary gas is at rest with respect to the earth so that p_d vanishes while p_0 remains finite. The exact solution for the latter case has been given recently by Slutz (ref. 6) and by Midgley and Davis (ref. 7). Comparisons in those papers show that all general features of the exact solution are approximated reasonably well, although the exact solution indicates that the boundary dips in considerably deeper at the point over the pole. The exact solution must, in fact, display a sharp cusp at this point in order to preserve a nonvanishing value for B_z . The cusp is not

revealed correctly by the present approximation, nor perfectly by the essentially exact numerical solutions of Slutz or Midgley and Davis. Probably the best representation of the conditions that prevail in the vicinity of the neutral points when $p_o \neq 0$ is to be had by examination of the exact analytic solution for the corresponding two-dimensional problem for $p_d = 0$ given by Cole and Huth in reference 15. Their solution indicates that the shape of the boundary for the case considered is described by a nephroid, that is, an epicycloid in which the radius of the rolling circle is half that of the fixed circle. Slutz also gives numerical values resulting from a comparison of the geocentric distances to the boundary in the equatorial plane and notes that, with $f = 1$, the approximate solution underestimates the distance by 9 percent. On the other hand, similar comparisons by Hurley (ref. 16) and by Spreiter and Briggs (refs. 2, 3, and 4) for the case $p_o = 0$ and $p_d \neq 0$ for the analogous two-dimensional problem show that the distance along the sun-earth line is overestimated by about 5 percent.

The determination of the solution for the remainder of the meridian plane where the boundary is exposed to the stream requires consideration of equation (12). This equation can be rewritten as follows upon solving for $d\rho/d\theta$

$$\frac{d\rho}{d\theta} = \frac{\rho[-(2 + \rho^6)\sin\theta \cos\theta]}{4 \cos^2\theta - \rho^6\left(\cos^2\theta + \frac{p_o}{p_d}\right)} \pm \frac{\rho^4 \sqrt{9 \sin^2\theta \cos^2\theta + \frac{p_o}{p_d} \left[1 + 3 \cos^2\theta - \rho^6\left(1 + \frac{p_o}{p_d}\right)\right]}}{4 \cos^2\theta - \rho^6\left(\cos^2\theta + \frac{p_o}{p_d}\right)} \quad (16)$$

When $p_o/p_d = 0$, equation (16) reduces to

$$\frac{d\rho}{d\theta} = \rho \tan\theta \left(\frac{\rho^3 \mp 1}{\rho^3 \pm 2} \right) \quad (17)$$

and the solution is as described in detail in references 2 and 3. For the general case in which $p_o/p_d \neq 0$, all integral curves representing real solutions are confined to the interior of the region bounded by the limiting line defined by

$$\rho = \left[\frac{9 \sin^2\theta \cos^2\theta + \frac{p_o}{p_d}(1 + 3 \cos^2\theta)}{\frac{p_o}{p_d} \left(1 + \frac{p_o}{p_d}\right)} \right]^{1/6} \quad (18)$$

Plots of the integral curves of equation (16) with both the upper (plus) and lower (minus) sign are shown in figure 6 for the case $p_o/p_d = 1$. Of all these curves, only one from figure 6(a) crosses the y axis normal to the direction of the incident stream and at a finite distance from the dipole singularity. Since it is also tangent to the limiting contour at this point, the value for ρ can

be obtained from equation (18) if the equal sign is used and θ is equated to $\pi/2$. The result is

$$\rho = \left(1 + \frac{p_o}{p_d}\right)^{-1/6} \quad (19)$$

which agrees with the corresponding value obtained by considering the integral curves for the equatorial plane. The integral curve shown in figure 6(a) that passes through the value for ρ given by equation (19) at $\theta = \pi/2$ can be used, at most, to represent the solution as far toward the polar axis as the point at which $dz/dy = 0$. It cannot be used for points nearer the polar axis because the boundary is shielded from the stream, and the desired solution must be represented by an integral curve of equation (14) rather than (16).

Considerations described above provide curves to represent traces of the portions of the boundary in the vicinity of both points of intersection with the sun-earth line. There remains the task of joining the two curves to complete the determination of the trace of the boundary in the meridian plane. This must be done, for the case $p_o/p_d = 1$, by employing segments of integral curves from figure 5 in shielded regions and from figure 6 in exposed regions. This can be accomplished in a unique and physically satisfying manner by imposing the condition that transition from the integral curve of figure 5(a) selected to represent the shielded region on the nighttime side of the earth to a curve from figure 6(a) is made at the point where the boundary is parallel to the direction of the incident stream. Thus, $dz/dy = 0$ at the point where the two curves are joined; hence, $\cos \psi = 0$, and equations (2a) and (2b) coalesce into one at this point. The curve so chosen, together with its possible continuous extension across the z axis selected from the integral curves of figure 6(b), defines the continuation of the trace in the upstream direction until the point is reached at which the boundary is shielded from the stream by portions even further upstream. The segment of the boundary next upstream is therefore defined by the connecting integral curve from figure 5(b). The remainder of the trace of the boundary is defined by the integral curve from figure 5(a) that can be joined to the trace of the nose portion of the boundary from figure 6(a) at the point where both are parallel to the direction of the incident stream. The result is displayed in figure 7. The point of intersection of the last two curves to be defined corresponds to a neutral point of the exact solution of the Chapman-Ferraro problem toward which all field lines in the boundary converge, turn abruptly, and extend to the earth. The intensity of the magnetic field should, moreover, be zero at such a point. Although these conditions are not fully realized in the present approximate solutions, the magnetic field vectors, and hence also the currents, are directed oppositely on the two sides of the neutral point. This condition provides, in fact, the physical basis for the choice of the particular combination of segments of integral curves described above, since no other connected combination of curves satisfied this condition. As noted for the case in which $p_d = 0$ and $p_o \neq 0$, the boundary should be sharply cusped inward toward the earth at the neutral points if $p_o \neq 0$. It can be seen, however, that the approximate solution provides only sharp corners at these points.

The procedure just described is sufficient to provide unique solutions that satisfactorily approximate the principal physical requirements of the problem for all values for p_o/p_d greater than about unity. For values for p_o/p_d less

than unity, however, the sheltered region near the polar axis disappears and it is not necessary to include this feature in the solution. This is undoubtedly a consequence of the approximation introduced by the use of equation (3), since, in the exact solution, a shielded region must always develop in the vicinity of the neutral point when $p_o \neq 0$.

For values of p_o/p_d less than about 0.1, a new situation develops. In this case, the integral curve of equation (16) that can be joined to the curve for the shielded segment of the boundary on the nighttime side of the earth at the point where the curves are parallel to the direction of the incident stream does not extend across the polar axis. The reason is associated with the fact that the limiting curve defined by equation (18) dips sharply toward the origin along the polar axis, as illustrated for the case $p_o/p_d = 0.01$ in figure 8. More detailed inspection of the integral curves in the immediate vicinity of this axis, as illustrated for the same case in figure 9, reveals, however, that only one curve which joins the exposed and shielded segments of the boundary can be constructed from the possible integral curves. It is composed of segments of the integral curves that are tangent to the limiting curve on the downstream side of the polar axis together with their continuous extension onto the upstream side of the axis. This procedure is used, therefore, to construct the polar portion of the trace of the boundary for all values for p_o/p_d less than about 0.1. The results are shown in figure 7. It should be observed that the corner that develops on the downstream side of the polar axis cannot occur in an exact solution since B_g would vanish there and equation (2) would not be satisfied. It appears in the present solution, however, as a result of the use of the approximation given by equation (3).

The procedure just described for small p_o/p_d goes smoothly over into that used previously in references 2 and 3 for the case $p_o/p_d = 0$. For the latter case, the geocentric distances to the limiting curve defined by equation (18) increase to infinity except along the y and z axes where the limiting curve degenerates into straight lines extending from infinity to values for ρ of 1 and $2^{1/3}$, respectively. The latter points correspond to the singular points of equation (17) to which equation (16) degenerates as p_o/p_d vanishes. The separated curves in the upper lobes of figures 8 and 9 thus merge into the connected and continuous integral curves of equation (17) shown previously in references 2 and 3, and the tangency condition used to select the integral curve to represent the trace of the boundary in the polar regions degenerates into the simpler condition of merely passing through the singular point at $\theta = 0$, $\rho = 2^{1/3}$. This result is also included for completeness in figure 7. The procedures described above thus provide a complete and logical transition between the procedures required to determine results for each of the limiting cases, $p_d = 0$ and $p_o = 0$. The numerical results are presented in tabular form in table II.

Results presented in the manner of figures 4 and 7 in terms of values for ρ for various p_o/p_d portray the relative dimensions of the boundary of the geomagnetic field as they would appear if p_d is held fixed while p_o is varied. It is of interest to consider the converse in which p_o is held fixed while p_d is varied. The results presented in figure 7 are shown in this way in figure 10 by plotting values for $\rho(p_o/p_d)^{1/6}$ for various p_o/p_d .

Finally, figure 11 is presented to provide a somewhat better picture of the three-dimensional aspects of the solution.

SOLUTION FOR THE MERIDIAN PLANE CONTAINING THE SUN-EARTH LINE, $\lambda \neq 0$

The determination of the trace of the boundary of the geomagnetic field in the meridian plane containing the sun-earth line for the case in which the dipole axis is not normal to the direction of the incident stream requires solution of equation (4) with ϕ equated to $\pm\pi/2$ and $\partial\rho/\partial\phi$ to zero. Equation (4a) thus becomes

$$\begin{aligned} \frac{1}{\rho^6} \left(\sin \theta + \frac{2 \cos \theta}{\rho} \frac{d\rho}{d\theta} \right)^2 &= \frac{p_0}{p_d} \left[1 + \left(\frac{1}{\rho} \frac{d\rho}{d\theta} \right)^2 \right] + \left[S \sin \theta \cos \lambda - \cos \theta \sin \lambda \right. \\ &\quad \left. - \frac{1}{\rho} \frac{d\rho}{d\theta} (S \cos \theta \cos \lambda + \sin \theta \sin \lambda) \right]^2 \end{aligned} \quad (20)$$

where S is used to represent $\sin(\pm\pi/2) = \pm 1$, and equation (4b) remains unchanged.

Equation (4b) is independent of λ , and the discussion of its solution for the present applications is identical to that already given following equations (13), (14), and (15) for $\lambda = 0$. Equation (20), on the other hand, depends on λ . Although the complexity is greater, the general form of equation (20) is similar to that of equation (12) for $\lambda = 0$, and similar techniques may be applied to determine the solution. Thus, equation (20) is first rewritten as follows by solving for $d\rho/d\theta$ and rearranging:

$$\begin{aligned} \frac{d\rho}{d\theta} &= \left\{ 4 \cos^2 \theta - \rho^6 \left[\frac{p_0}{p_d} + \cos^2(\theta - \lambda S) \right] \right\}^{-1} \left\{ -\frac{\rho}{2} [2 \sin 2\theta + \rho^6 \sin 2(\theta - \lambda S)] \right. \\ &\quad \left. \pm \rho^4 \sqrt{[2 \sin(\theta - \lambda S) \cos \theta + \cos(\theta - \lambda S) \sin \theta]^2 + \frac{p_0}{p_d} \left[1 + 3 \cos^2 \theta - \rho^6 \left(1 + \frac{p_0}{p_d} \right) \right]} \right\} \end{aligned} \quad (21)$$

When $p_0/p_d = 0$, equation (21) reduces to

$$\frac{d\rho}{d\theta} = \rho \frac{\rho^3 \sin(\theta - \lambda S) \mp \sin \theta}{\rho^3 \cos(\theta - \lambda S) \pm 2 \cos \theta} \quad (22)$$

the analytic and numerical solution of which is described in detail in references 2 and 3. For the general case in which $p_o/p_d \neq 0$, no analytic solution has been found and it is necessary to resort to numerical techniques.

As for $\lambda = 0$, all integral curves of equation (21) are confined to the interior of a finite region, the boundary of which is defined by equating to zero the radicand in equation (21), that is, by

$$\rho = \left\{ \frac{[2 \sin(\theta - \lambda S) \cos \theta + \cos(\theta - \lambda S) \sin \theta]^2 + (p_o/p_d)(1 + 3 \cos^2 \theta)}{(p_o/p_d)[1 + (p_o/p_d)]} \right\}^{1/6} \quad (23)$$

Plots of the limiting lines defined by equation (23) are illustrated in figure 12 for several different values for p_o/p_d and two values for λ , namely 11.5° and 34.5° . The integral curves of equation (21) for any given set of values for p_o/p_d and λ are similar in general form to those illustrated for $\lambda = 0$ in figures 6, 8, and 9, although skewed an amount that depends on the value for λ . There is, in particular, only one integral curve that is suitable to represent the portion of the boundary nearest the sun, since all others either terminate at the limiting line or extend to the origin. There is also, for a similar reason, only one integral curve of equation (4b) or (14) that can be used to represent the shielded portion of the boundary farthest from the sun. With these portions of the boundary fixed, there remains for any given case only one combination of integral curves of equations (14) and (21) that can be joined satisfactorily to complete the meridian trace of the boundary. Although the precise numerical details depend on the values for p_o/p_d and λ , the procedures are completely analogous to those described in the preceding section for $\lambda = 0$.

The final results for $p_o/p_d = 1$ and $\lambda = 11.5^\circ$ and 34.5° are shown in figure 13 together with the limiting lines defined by equation (23). The corresponding results for $p_o/p_d = 0.01$ are shown in figure 14. As noted in the figure legend, the limiting lines are indicated by dotted lines, the exposed portions of the boundary calculated using equation (21) are indicated by solid lines, and the shielded portions calculated using equation (14) are indicated by dashed lines. The points at which the latter two portions of the boundary join are indicated by small circles in the same manner as in figure 7. As for $\lambda = 0$, the results for $p_o/p_d = 1$ properly display smooth transitions between the curves representing the exposed and shielded portions of the boundary. They also indicate the presence of a small shielded region near the upper neutral point. As noted previously, such features must also characterize the form of the boundary that would be indicated by an exact solution of the steady-state Chapman-Ferraro problem in which the approximation indicated by equation (3) is not introduced. As typified by the results for $p_o/p_d = 0.01$ shown in figure 14, it is, however, not possible to continue to satisfy these conditions in the approximate solution as p_o/p_d approaches zero. For such cases, the sharp dip in the limiting curve that occurs at high latitudes becomes the controlling feature in the selection of the integral curves to represent the portions of the boundary downwind from the neutral points. Results obtained in this way merge smoothly into those for $p_o/p_d = 0$ given in references 2 and 3, and form a complete and continuously changing set

extending between the two limiting cases, $p_d = 0$ and $p_o = 0$. The numerical results are presented in table II, and illustrated graphically in figure 15. The coordinates of the neutral points are of special interest and are listed separately in table III.

CONCLUDING REMARKS

It is anticipated that the results of the present investigation display most of the principal features contained in an exact solution of the same problem. The geocentric distance along the sun-earth line to the boundary of the geomagnetic field may be overestimated by a few percent on the daytime side of the earth and underestimated by a few percent on the nighttime side. The error on the nighttime side is, in general, probably slightly greater than the value of 9 percent given by Slutz (ref. 6) for $p_d = 0$, since the neutral point is on the daytime side and the approximation introduced by use of equation (3) does not properly take into account the fact that somewhat more than half the magnetic flux is deflected into the nighttime side of the cavity. It is noted further that the boundary should contain a sharp cusp directed toward the earth at each neutral point for all values for p_o/p_d except zero. For the latter case, the boundary must be parallel to the direction of the incident stream at the neutral points. The corners that develop in the present results for small p_o/p_d at the points where the curves for the exposed and shielded regions join on the nighttime side of the earth cannot occur in an exact solution, but are the result of the approximation introduced by using equation (3). It is anticipated, however, that this shortcoming of the approximate solution is essentially local in character.

Ames Research Center
National Aeronautics and Space Administration
Moffett Field, Calif., May 17, 1963

APPENDIX

PRINCIPAL SYMBOLS

a	radius of earth, cm
B	total magnetic field, gauss
B'	magnetic field due to currents in boundary, gauss
B_p	permanent magnetic field, gauss
B_{p0}	intensity of geomagnetic field at equator, ≈ 0.312 gauss
B_s	intensity of field at the boundary, gauss
B_t	tangential component of the geomagnetic dipole field at the boundary, gauss
f	proportionality constant introduced in approximate boundary condition (see eq. (3))
M_p	dipole moment of earth = $a^3 B_{p0}$
m	mass of proton $\approx 1.67 \times 10^{-24}$ gm
n	number of protons per cm^3
p_0	static pressure of the interplanetary gas
p_d	dynamic pressure of the incident stream = $2mnv^2$
r, φ, θ	spherical coordinates (see fig. 1)
r_0	unit of length defined by equation (5)
R	$\rho(p_0/p_d)^{1/6}$
S	$\sin(\pm\pi/2) = \pm 1$
v	velocity of plasma, cm/sec
x, y, z	rectangular coordinates (see fig. 1)
\hat{l}_θ	unit vector in the direction of increasing θ
\hat{l}_r	unit vector in the radial direction
λ	angle between direction of the incident stream and the geomagnetic equatorial plane (see fig. 1)

ρ

$$\frac{r}{r_0}$$

ψ

angle between direction of the incident stream and the outward normal
to the surface (see fig. 1)

REFERENCES

1. Beard, David B.: The Interaction of the Terrestrial Magnetic Field with the Solar Corpuscular Radiation. Jour. Geophys. Res., vol. 65, no. 11, Nov. 1960, pp. 3559-3568.
2. Spreiter, John R., and Briggs, Benjamin R.: Theoretical Determination of the Form of the Hollow Produced in the Solar Corpuscular Stream by Interaction With the Magnetic Dipole Field of the Earth. NASA TR R-120, 1961.
3. Spreiter, John R., and Briggs, Benjamin R.: Theoretical Determination of the Form of the Boundary of the Solar Corpuscular Stream Produced by Interaction With the Magnetic Dipole Field of the Earth. Jour. Geophys. Res., vol. 67, no. 1, Jan. 1962, pp. 37-51.
4. Spreiter, John R., and Briggs, Benjamin R.: On the Choice of Condition to Apply at the Boundary of the Geomagnetic Field in the Steady-State Chapman-Ferraro Problem. Jour. Geophys. Res., vol. 67, no. 7, July 1962, pp. 2983-2985.
5. Spreiter, John R., and Hyett, B. Jeanne: The Effect of a Uniform External Pressure on the Boundary of the Geomagnetic Field in a Steady Solar Wind. Jour. Geophys. Res., vol. 68, no. 6, March 15, 1963, pp. 1631-1642.
6. Slutz, Ralph J.: The Shape of the Geomagnetic Field Boundary under Uniform External Pressure. Jour. Geophys. Res., vol. 67, no. 2, Feb. 1962, pp. 505-513.
7. Midgley, James E., and Davis, Leverett, Jr.: Computation of the Bounding Surface of a Dipole Field in a Plasma by a Moment Technique. Jour. Geophys. Res., vol. 67, no. 2, Feb. 1962, pp. 499-504.
8. Ferraro, V. C. A.: An Approximate Method of Estimating the Size and Shape of the Stationary Hollow Carved out in a Neutral Ionized Stream of Corpuscles Impinging on the Geomagnetic Field. Jour. Geophys. Res., vol. 65, no. 12, Dec. 1960, pp. 3951-3953.
9. Davis, Leverett, Jr., and Beard, David B.: A Correction to the Approximate Condition for Locating the Boundary between a Magnetic Field and a Plasma. Jour. Geophys. Res., vol. 67, no. 11, Oct. 1962, pp. 4505-4507.
10. Chapman, Sydney: Idealized Problems of Plasma Dynamics Relating to Geomagnetic Storms. Reviews of Modern Physics, vol. 32, no. 4, Oct. 1960, pp. 919-933.
11. Chapman, S.: Solar Plasma, Geomagnetism and Aurora. Geophysics, The Earth's Environment. C. DeWitt, J. Hieblot, and A. Lebeau, ed., Gordon and Breach, New York, 1963, pp. 371-502.

12. Dungey, J. W.: Cosmic Electrodynamics. Cambridge University Press, Cambridge, 1958.
13. Neugebauer, Marcia, and Snyder, Conway W.: The Mission of Mariner II: Preliminary Observations, Solar Plasma Experiment. Science, vol. 138, no. 3545, Dec. 7, 1962, pp. 1095-1097.
14. Beard, David B.: The Interaction of the Terrestrial Magnetic Field with the Solar Corpuscular Radiation, 2. Second-Order Approximation. Jour. Geophys. Res., vol. 67, no. 2, Feb. 1962, pp. 477-483.
15. Cole, J. D., and Huth, J. H.: Some Interior Problems of Hydromagnetics. Physics of Fluids, vol. 2, no. 6, Nov.-Dec. 1959, pp. 624-626.
16. Hurley, James: Interaction of a Streaming Plasma with the Magnetic Field of a Two-Dimensional Dipole. Physics of Fluids, vol. 4, no. 7, July 1961, pp. 854-859.

TABLE I.- COORDINATES φ AND ρ OF BOUNDARY OF HOLLOW IN THE EQUATORIAL PLANE FOR
VARIOUS p_o/p_d , $\lambda = 0$

φ , deg	p_o/p_d												
	0.	0.01	0.05	0.1	0.2	0.3	0.4	0.5	1.	2.	5.	10.	100.
	θ , deg												
90	1.000	0.998	0.992	0.984	0.970	0.957	0.945	0.935	0.891	0.833	0.742	0.671	0.463
95	1.001	0.999	0.993	0.985	0.971	0.958	0.946	0.935	0.891	0.833	0.742	0.671	0.463
100	1.003	1.002	0.995	0.987	0.973	0.960	0.948	0.937	0.893	0.834	0.742	0.671	0.463
105	1.007	1.005	0.999	0.991	0.976	0.963	0.951	0.940	0.895	0.835	0.743	0.671	0.463
110	1.013	1.011	1.004	0.996	0.981	0.967	0.955	0.944	0.898	0.837	0.744	0.672	0.463
115	1.020	1.018	1.011	1.003	0.987	0.973	0.961	0.949	0.902	0.840	0.745	0.672	0.463
120	1.030	1.028	1.020	1.011	0.995	0.981	0.967	0.955	0.906	0.843	0.747	0.673	0.463
125	1.041	1.039	1.031	1.021	1.004	0.989	0.975	0.963	0.912	0.846	0.748	0.674	0.463
130	1.054	1.052	1.043	1.033	1.015	0.999	0.985	0.971	0.918	0.851	0.750	0.675	0.463
135	1.069	1.067	1.058	1.047	1.028	1.011	0.995	0.981	0.925	0.855	0.752	0.676	0.463
140	1.087	1.084	1.074	1.063	1.042	1.024	1.007	0.992	0.933	0.860	0.754	0.677	0.464
145	1.107	1.100	1.093	1.081	1.059	1.039	1.021	1.005	0.942	0.865	0.755	0.678	0.464
150	1.130	1.127	1.115	1.102	1.077	1.055	1.036	1.018	0.951	0.870	0.758	0.679	0.464
155	1.156	1.152	1.140	1.125	1.097	1.073	1.052	1.033	0.960	0.875	0.760	0.679	0.464
160	1.185	1.181	1.167	1.150	1.120	1.093	1.070	1.049	0.970	0.880	0.761	0.680	0.464
165	1.219	1.214	1.198	1.179	1.145	1.115	1.089	1.065	0.980	0.884	0.763	0.680	0.464
170	1.258	1.252	1.233	1.211	1.172	1.138	1.109	1.083	0.989	0.888	0.764	0.681	0.464
175	1.299	1.294	1.272	1.247	1.202	1.163	1.129	1.100	0.996	0.890	0.765	0.681	0.464
180	1.349	1.342	1.316	1.286	1.233	1.188	1.149	1.115	1.000	0.891	0.765	0.681	0.464
185	1.405	1.397	1.366	1.330	1.267	1.212	1.164	1.122	1.000	0.891	0.765	0.681	0.464
190	1.470	1.460	1.422	1.378	1.299	1.222	1.164	1.122	1.000	0.891	0.765	0.681	0.464
195	1.544	1.532	1.484	1.429	1.308	1.222	1.164	1.122	1.000	0.891	0.765	0.681	0.464
200	1.631	1.615	1.554	1.468	1.308	1.222	1.164	1.122	1.000	0.891	0.765	0.681	0.464
205	1.733	1.712	1.630	1.468	1.308	1.222	1.164	1.122	1.000	0.891	0.765	0.681	0.464
210	1.853	1.825	1.648	1.468	1.308	1.222	1.164	1.122	1.000	0.891	0.765	0.681	0.464
215	1.997	1.958	1.648	1.468	1.308	1.222	1.164	1.122	1.000	0.891	0.765	0.681	0.464
220	2.172	2.113	1.648	1.468	1.308	1.222	1.164	1.122	1.000	0.891	0.765	0.681	0.464
225	2.388	2.154	1.648	1.468	1.308	1.222	1.164	1.122	1.000	0.891	0.765	0.681	0.464
230	2.661	2.154	1.648	1.468	1.308	1.222	1.164	1.122	1.000	0.891	0.765	0.681	0.464
235	3.016	2.154	1.648	1.468	1.308	1.222	1.164	1.122	1.000	0.891	0.765	0.681	0.464
240	3.492	2.154	1.648	1.468	1.308	1.222	1.164	1.122	1.000	0.891	0.765	0.681	0.464
245	4.164	2.154	1.648	1.468	1.308	1.222	1.164	1.122	1.000	0.891	0.765	0.681	0.464
250	5.177	2.154	1.648	1.468	1.308	1.222	1.164	1.122	1.000	0.891	0.765	0.681	0.464
255	6.874	2.154	1.648	1.468	1.308	1.222	1.164	1.122	1.000	0.891	0.765	0.681	0.464
260		2.154	1.648	1.468	1.308	1.222	1.164	1.122	1.000	0.891	0.765	0.681	0.464
265		2.154	1.648	1.468	1.308	1.222	1.164	1.122	1.000	0.891	0.765	0.681	0.464
270		2.154	1.648	1.468	1.308	1.222	1.164	1.122	1.000	0.891	0.765	0.681	0.464

TABLE II. - COORDINATES θ AND ρ OF BOUNDARY OF HOLLOW IN THE MERIDIAN PLANE
CONTAINING THE DIPOLE AXIS AND THE SUN-EARTH LINE FOR VARIOUS p_0/p_d
(a) $\lambda = 0$

θ , deg	p_0/p_d												
	0.	0.01	0.05	0.1	0.2	0.3	0.4	0.5	1.	2.	5.	10.	100.
$\varphi = \pi/2$													
0	1.260	1.254	1.229	1.181	1.065	0.997	0.951	0.917	0.818	0.729	0.626	0.558	0.380
5	1.186	1.180	1.159	1.124	1.028	0.967	0.924	0.891	0.798	0.728	0.634	0.568	0.389
10	1.116	1.111	1.093	1.066	0.988	0.933	0.893	0.875	0.813	0.742	0.648	0.581	0.398
15	1.051	1.047	1.031	1.008	0.944	0.921	0.902	0.886	0.825	0.755	0.660	0.592	0.406
20	1.000	0.997	0.985	0.972	0.948	0.928	0.910	0.894	0.836	0.767	0.672	0.603	0.413
25	1.000	0.997	0.987	0.974	0.953	0.934	0.917	0.902	0.845	0.777	0.682	0.612	0.420
30	1.000	0.997	0.988	0.977	0.956	0.938	0.922	0.908	0.853	0.787	0.691	0.621	0.427
35	1.000	0.998	0.989	0.978	0.959	0.942	0.927	0.913	0.860	0.795	0.700	0.629	0.432
40	1.000	0.998	0.989	0.979	0.961	0.945	0.931	0.918	0.866	0.802	0.708	0.637	0.438
45	1.000	0.998	0.990	0.981	0.963	0.948	0.934	0.921	0.872	0.808	0.714	0.643	0.443
50	1.000	0.998	0.990	0.981	0.965	0.950	0.937	0.924	0.876	0.814	0.720	0.649	0.447
55	1.000	0.998	0.991	0.982	0.966	0.952	0.939	0.927	0.880	0.818	0.725	0.654	0.451
60	1.000	0.998	0.991	0.983	0.967	0.953	0.941	0.929	0.883	0.822	0.730	0.659	0.454
65	1.000	0.998	0.991	0.983	0.968	0.955	0.942	0.931	0.885	0.826	0.734	0.662	0.457
70	1.000	0.998	0.992	0.984	0.969	0.956	0.943	0.932	0.887	0.828	0.737	0.665	0.459
75	1.000	0.998	0.992	0.984	0.969	0.956	0.944	0.933	0.889	0.830	0.739	0.668	0.461
80	1.000	0.998	0.992	0.984	0.970	0.957	0.945	0.934	0.890	0.832	0.741	0.669	0.462
85	1.000	0.998	0.992	0.984	0.970	0.957	0.945	0.935	0.891	0.832	0.742	0.670	0.463
90	1.000	0.998	0.992	0.984	0.970	0.957	0.945	0.935	0.891	0.833	0.742	0.670	0.463
95	1.000	0.998	0.992	0.984	0.970	0.957	0.945	0.935	0.891	0.832	0.742	0.670	0.463
100	1.000	0.998	0.992	0.984	0.970	0.957	0.945	0.934	0.890	0.832	0.741	0.669	0.462
105	1.000	0.998	0.992	0.984	0.969	0.956	0.944	0.933	0.889	0.830	0.739	0.668	0.461
110	1.000	0.998	0.992	0.984	0.969	0.956	0.943	0.932	0.887	0.828	0.737	0.665	0.459
115	1.000	0.998	0.991	0.983	0.968	0.955	0.942	0.931	0.885	0.826	0.734	0.662	0.457
120	1.000	0.998	0.991	0.983	0.967	0.953	0.941	0.929	0.883	0.822	0.730	0.659	0.454
125	1.000	0.998	0.991	0.982	0.966	0.952	0.939	0.927	0.880	0.818	0.725	0.654	0.451
130	1.000	0.998	0.990	0.981	0.965	0.950	0.937	0.924	0.876	0.814	0.720	0.649	0.447
135	1.000	0.998	0.990	0.981	0.963	0.948	0.934	0.921	0.872	0.808	0.714	0.643	0.443
140	1.000	0.998	0.989	0.979	0.961	0.945	0.931	0.918	0.866	0.802	0.708	0.637	0.438
145	1.000	0.998	0.989	0.978	0.959	0.942	0.927	0.913	0.860	0.795	0.700	0.629	0.432
150	1.000	0.997	0.988	0.977	0.956	0.938	0.922	0.908	0.853	0.787	0.691	0.621	0.427
155	1.000	0.997	0.987	0.974	0.953	0.934	0.917	0.902	0.845	0.777	0.682	0.612	0.420
160	1.000	0.997	0.985	0.972	0.948	0.928	0.910	0.894	0.836	0.767	0.672	0.603	0.413
165	1.000	1.047	1.031	1.008	0.944	0.921	0.902	0.886	0.825	0.755	0.660	0.592	0.406
170	1.051	1.111	1.093	1.066	0.988	0.933	0.893	0.875	0.813	0.742	0.648	0.581	0.398
175	1.186	1.180	1.159	1.124	1.028	0.967	0.924	0.891	0.798	0.728	0.634	0.568	0.389
180	1.260	1.254	1.229	1.181	1.065	0.997	0.951	0.917	0.818	0.729	0.626	0.558	0.380
$\varphi = -\pi/2$													
0	1.260	1.254	1.229	1.181	1.065	0.997	0.951	0.917	0.818	0.729	0.626	0.558	0.380
5	1.341	1.334	1.304	1.226	1.095	1.024	0.976	0.941	0.838	0.747	0.641	0.571	0.389
10	1.430	1.421	1.386	1.258	1.121	1.048	0.998	0.962	0.857	0.764	0.655	0.584	0.398
15	1.528	1.517	1.442	1.284	1.144	1.069	1.019	0.982	0.875	0.779	0.669	0.596	0.406
20	1.639	1.625	1.468	1.307	1.165	1.089	1.038	1.000	0.891	0.794	0.681	0.607	0.413
25	1.764	1.746	1.492	1.330	1.185	1.107	1.055	1.017	0.906	0.807	0.693	0.617	0.420
30	1.907	1.883	1.515	1.350	1.203	1.124	1.072	1.032	0.920	0.819	0.703	0.627	0.427
35	2.075	2.013	1.537	1.369	1.220	1.140	1.087	1.047	0.933	0.831	0.713	0.635	0.433
40	2.273	2.035	1.555	1.386	1.235	1.154	1.100	1.060	0.944	0.841	0.722	0.643	0.438
45	2.514	2.057	1.573	1.402	1.249	1.167	1.113	1.072	0.955	0.851	0.730	0.651	0.443
50	2.814	2.078	1.589	1.416	1.261	1.179	1.124	1.083	0.964	0.859	0.738	0.657	0.448
55	3.197	2.096	1.603	1.428	1.272	1.189	1.133	1.092	0.973	0.867	0.744	0.663	0.452
60	3.707	2.111	1.615	1.438	1.281	1.198	1.142	1.100	0.980	0.873	0.749	0.668	0.455
65	4.420	2.125	1.625	1.447	1.289	1.205	1.149	1.107	0.986	0.879	0.754	0.672	0.458
70	5.492	2.135	1.633	1.455	1.296	1.211	1.155	1.112	0.991	0.883	0.758	0.675	0.460
75	7.283	2.144	1.639	1.460	1.301	1.216	1.159	1.117	0.995	0.886	0.761	0.678	0.462
80		2.150	1.644	1.465	1.305	1.219	1.162	1.120	0.998	0.889	0.763	0.680	0.463
85		2.153	1.647	1.467	1.307	1.222	1.164	1.122	0.999	0.890	0.764	0.681	0.464
90		2.154	1.648	1.468	1.308	1.222	1.165	1.122	1.000	0.891	0.765	0.681	0.464
95		2.153	1.647	1.467	1.307	1.222	1.164	1.122	0.999	0.890	0.764	0.681	0.464
100		2.150	1.644	1.465	1.305	1.219	1.162	1.120	0.998	0.889	0.763	0.680	0.463
105	7.283	2.144	1.639	1.460	1.301	1.216	1.159	1.117	0.995	0.886	0.761	0.678	0.462
110	5.492	2.135	1.633	1.455	1.296	1.211	1.155	1.112	0.991	0.883	0.758	0.675	0.460
115	4.420	2.125	1.625	1.447	1.289	1.205	1.149	1.107	0.986	0.879	0.754	0.672	0.458
120	3.707	2.111	1.615	1.438	1.281	1.198	1.142	1.100	0.980	0.873	0.749	0.668	0.455
125	3.197	2.096	1.603	1.428	1.272	1.189	1.133	1.092	0.973	0.867	0.744	0.663	0.452
130	2.814	2.078	1.589	1.416	1.261	1.179	1.124	1.083	0.964	0.859	0.738	0.657	0.448
135	2.514	2.057	1.573	1.402	1.249	1.167	1.113	1.072	0.955	0.851	0.730	0.651	0.443
140	2.273	1.556	1.556	1.386	1.235	1.154	1.100	1.060	0.944	0.841	0.722	0.643	0.438
145	2.075	1.986	1.537	1.369	1.220	1.140	1.087	1.047	0.933	0.831	0.713	0.635	0.433
150	1.907	1.883	1.516	1.350	1.203	1.124	1.072	1.032	0.920	0.819	0.703	0.627	0.427
155	1.764	1.746	1.492	1.330	1.185	1.107	1.055	1.017	0.906	0.807	0.693	0.617	0.420
160	1.639	1.625	1.468	1.307	1.165	1.089	1.038	1.000	0.891	0.794	0.681	0.607	0.413
165	1.528	1.517	1.457	1.284	1.144	1.069	1.019	0.982	0.875	0.779	0.669	0.596	0.406
170	1.430	1.421	1.386	1.258	1.121	1.048	0.998	0.962	0.857	0.764	0.655	0.584	0.398
175	1.341	1.334	1.304	1.226	1.095	1.024	0.976	0.941	0.838	0.747	0.641	0.571	0.389
180	1.260	1.254	1.229	1.181	1.065	0.997	0.951	0.917	0.818	0.729	0.626	0.558	0.380

TABLE II. - COORDINATES θ AND ρ OF BOUNDARY OF HOLLOW IN THE MERIDIAN PLANE CONTAINING THE DIPOLE AXIS AND THE SUN-EARTH LINE FOR VARIOUS p_0/p_d - Continued
(b) $\lambda = 5.75$

θ , deg	p_0/p_d												
	0.	0.01	0.05	0.1	0.2	0.3	0.4	0.5	1.	2.	5.	10.	100.
	$\varphi = \pi/2$												
0	1.325	1.317	1.285	1.197	1.069	1.000	0.953	0.919	0.819	0.729	0.626	0.558	0.380
5	1.240	1.234	1.216	1.152	1.037	0.972	0.927	0.894	0.804	0.731	0.635	0.569	0.389
10	1.164	1.158	1.138	1.096	1.000	0.940	0.904	0.885	0.819	0.745	0.649	0.581	0.398
15	1.092	1.088	1.071	1.038	0.960	0.936	0.915	0.897	0.832	0.759	0.662	0.593	0.406
20	1.026	1.028	1.017	0.993	0.966	0.943	0.923	0.906	0.843	0.771	0.673	0.603	0.413
25	1.023	1.017	1.004	0.994	0.969	0.948	0.930	0.913	0.853	0.782	0.684	0.613	0.420
30	1.021	1.018	1.007	0.995	0.972	0.952	0.935	0.919	0.861	0.791	0.693	0.622	0.427
35	1.019	1.016	1.006	0.995	0.974	0.955	0.939	0.924	0.868	0.799	0.702	0.630	0.433
40	1.017	1.015	1.005	0.995	0.975	0.957	0.942	0.928	0.873	0.806	0.709	0.638	0.438
45	1.015	1.013	1.004	0.994	0.976	0.959	0.944	0.931	0.878	0.812	0.715	0.644	0.443
50	1.014	1.011	1.003	0.994	0.976	0.960	0.946	0.933	0.882	0.818	0.722	0.650	0.447
55	1.012	1.010	1.002	0.993	0.976	0.961	0.947	0.935	0.885	0.822	0.727	0.655	0.451
60	1.010	1.008	1.001	0.992	0.976	0.961	0.948	0.936	0.888	0.825	0.731	0.659	0.454
65	1.009	1.007	1.000	0.991	0.975	0.961	0.948	0.937	0.890	0.828	0.735	0.663	0.457
70	1.007	1.005	0.998	0.990	0.975	0.961	0.949	0.937	0.891	0.830	0.738	0.666	0.459
75	1.006	1.004	0.997	0.989	0.974	0.961	0.948	0.937	0.892	0.832	0.740	0.668	0.461
80	1.004	1.002	0.996	0.988	0.973	0.960	0.948	0.937	0.892	0.833	0.741	0.670	0.462
85	1.003	1.001	0.994	0.987	0.972	0.959	0.947	0.936	0.892	0.833	0.742	0.670	0.463
90	1.001	0.999	0.993	0.985	0.971	0.958	0.946	0.935	0.891	0.833	0.742	0.671	0.463
95	1.000	0.998	0.992	0.984	0.970	0.957	0.945	0.934	0.891	0.832	0.741	0.670	0.463
100	0.998	0.997	0.990	0.982	0.968	0.955	0.944	0.933	0.889	0.831	0.740	0.669	0.462
105	0.997	0.995	0.989	0.981	0.967	0.954	0.942	0.931	0.887	0.829	0.738	0.667	0.461
110	0.995	0.994	0.987	0.979	0.965	0.952	0.940	0.929	0.885	0.827	0.735	0.665	0.459
115	0.994	0.992	0.985	0.978	0.963	0.950	0.938	0.927	0.882	0.824	0.733	0.662	0.457
120	0.992	0.991	0.984	0.976	0.961	0.947	0.935	0.924	0.879	0.820	0.729	0.658	0.454
125	0.991	0.989	0.982	0.974	0.959	0.945	0.932	0.921	0.875	0.816	0.724	0.654	0.451
130	0.989	0.987	0.980	0.972	0.956	0.942	0.929	0.918	0.871	0.811	0.719	0.648	0.447
135	0.988	0.986	0.978	0.969	0.953	0.939	0.926	0.914	0.866	0.805	0.713	0.643	0.443
140	0.986	0.984	0.976	0.967	0.950	0.935	0.921	0.909	0.860	0.798	0.706	0.636	0.438
145	0.984	0.982	0.974	0.964	0.947	0.931	0.917	0.904	0.854	0.791	0.698	0.629	0.432
150	0.982	0.980	0.971	0.961	0.943	0.925	0.911	0.898	0.847	0.783	0.690	0.620	0.427
155	0.980	0.978	0.969	0.958	0.938	0.921	0.905	0.892	0.839	0.774	0.680	0.612	0.420
160	0.978	0.976	0.966	0.954	0.933	0.914	0.898	0.884	0.829	0.763	0.670	0.602	0.413
165	1.014	1.011	0.997	0.979	0.928	0.907	0.890	0.875	0.818	0.752	0.659	0.591	0.406
170	1.074	1.070	1.054	1.033	0.972	0.923	0.886	0.854	0.806	0.739	0.647	0.580	0.398
175	1.138	1.133	1.114	1.090	1.015	0.959	0.918	0.887	0.794	0.725	0.633	0.568	0.389
180	1.204	1.202	1.178	1.148	1.055	0.992	0.948	0.915	0.817	0.729	0.626	0.558	0.380
$\varphi = -\pi/2$													
0	1.324	1.317	1.285	1.197	1.069	1.000	0.953	0.919	0.819	0.729	0.626	0.558	0.380
5	1.415	1.406	1.371	1.231	1.096	1.025	0.977	0.941	0.839	0.747	0.641	0.571	0.389
10	1.511	1.505	1.412	1.258	1.121	1.048	0.999	0.962	0.857	0.764	0.655	0.584	0.398
15	1.630	1.616	1.441	1.284	1.144	1.069	1.019	0.982	0.875	0.779	0.669	0.596	0.405
20	1.759	1.740	1.468	1.307	1.165	1.089	1.038	1.000	0.891	0.794	0.681	0.607	0.413
25	1.906	1.903	1.492	1.330	1.185	1.107	1.055	1.017	0.906	0.807	0.693	0.617	0.420
30	2.079	1.982	1.515	1.350	1.203	1.124	1.072	1.032	0.920	0.819	0.703	0.627	0.427
35	2.285	2.009	1.537	1.369	1.220	1.140	1.087	1.047	0.933	0.831	0.713	0.635	0.433
40	2.534	2.035	1.555	1.386	1.235	1.154	1.100	1.060	0.944	0.841	0.722	0.643	0.438
45	2.846	2.057	1.573	1.402	1.249	1.167	1.113	1.072	0.955	0.851	0.730	0.651	0.443
50	3.246	2.078	1.589	1.416	1.261	1.179	1.124	1.083	0.964	0.859	0.738	0.657	0.448
55	3.781	2.096	1.603	1.428	1.272	1.189	1.133	1.092	0.973	0.867	0.744	0.663	0.452
60	4.537	2.111	1.615	1.438	1.281	1.198	1.142	1.100	0.980	0.873	0.749	0.668	0.455
65	5.686	2.125	1.625	1.447	1.289	1.205	1.149	1.107	0.986	0.879	0.754	0.672	0.458
70	7.645	2.135	1.633	1.455	1.296	1.211	1.155	1.112	0.991	0.883	0.758	0.675	0.460
75		2.144	1.639	1.460	1.301	1.216	1.159	1.117	0.995	0.886	0.761	0.678	0.462
80		2.150	1.644	1.465	1.305	1.219	1.162	1.120	0.998	0.889	0.763	0.680	0.463
85		2.153	1.647	1.467	1.307	1.222	1.164	1.122	0.999	0.890	0.764	0.681	0.464
90		2.154	1.648	1.468	1.308	1.222	1.165	1.122	1.000	0.891	0.765	0.681	0.464
95		2.153	1.647	1.467	1.307	1.222	1.164	1.122	0.999	0.890	0.764	0.681	0.464
100	6.941	2.150	1.644	1.465	1.305	1.219	1.162	1.120	0.998	0.889	0.763	0.680	0.463
105	5.302	2.144	1.639	1.460	1.301	1.216	1.159	1.117	0.995	0.886	0.761	0.678	0.462
110	4.303	2.135	1.633	1.455	1.296	1.211	1.155	1.112	0.991	0.883	0.758	0.675	0.460
115	3.629	2.125	1.625	1.447	1.289	1.205	1.149	1.107	0.986	0.879	0.754	0.672	0.458
120	3.145	2.111	1.615	1.438	1.281	1.199	1.142	1.100	0.980	0.873	0.749	0.668	0.455
125	2.778	2.096	1.603	1.428	1.272	1.189	1.133	1.092	0.973	0.867	0.744	0.663	0.452
130	2.491	2.078	1.589	1.416	1.261	1.179	1.124	1.083	0.964	0.859	0.738	0.657	0.448
135	2.259	2.057	1.573	1.402	1.249	1.167	1.113	1.072	0.955	0.851	0.730	0.651	0.443
140	2.067	2.035	1.556	1.386	1.235	1.154	1.100	1.060	0.944	0.841	0.722	0.643	0.438
145	1.905	1.881	1.537	1.369	1.220	1.140	1.087	1.047	0.933	0.831	0.713	0.635	0.433
150	1.766	1.748	1.516	1.350	1.203	1.124	1.072	1.032	0.920	0.819	0.703	0.627	0.427
155	1.645	1.631	1.492	1.330	1.185	1.107	1.055	1.017	0.906	0.807	0.693	0.617	0.420
160	1.538	1.527	1.468	1.307	1.165	1.089	1.038	1.000	0.891	0.794	0.681	0.607	0.413
165	1.442	1.433	1.397	1.283	1.144	1.069	1.019	0.982	0.875	0.779	0.669	0.596	0.406
170	1.356	1.348	1.318	1.254	1.119	1.047	0.998	0.962	0.857	0.764	0.655	0.584	0.398
175	1.277	1.279	1.245	1.207	1.090	1.021	0.974	0.939	0.838	0.747	0.641	0.571	0.389
180	1.204	1.204	1.178	1.148	1.055	0.992	0.948	0.915	0.817	0.729	0.626	0.558	0.380

TABLE II. - COORDINATES θ AND ρ OF BOUNDARY OF HOLLOW IN THE MERIDIAN PLANE CONTAINING THE DIPOLE AXIS AND THE SUN-EARTH LINE FOR VARIOUS p_0/p_d - Continued
(c) $\lambda = 11.50$

	P_0/P_d												
θ , deg	0.	0.01	0.05	0.1	0.2	0.3	0.4	0.5	1.	2.	5.	10.	100.
$\varphi = \pi/2$													
0	1.397	1.391	1.349	1.201	1.071	1.001	0.954	0.919	0.819	0.729	0.626	0.558	0.380
5	1.304	1.307	1.267	1.166	1.042	0.974	0.929	0.895	0.809	0.733	0.637	0.569	0.389
10	1.218	1.212	1.204	1.120	1.008	0.945	0.916	0.895	0.824	0.748	0.650	0.582	0.398
15	1.139	1.134	1.116	1.065	0.979	0.951	0.928	0.908	0.838	0.762	0.663	0.593	0.406
20	1.066	1.070	1.054	1.016	0.985	0.959	0.937	0.918	0.850	0.775	0.675	0.604	0.413
25	1.051	1.044	1.030	1.016	0.988	0.964	0.944	0.926	0.860	0.786	0.685	0.614	0.420
30	1.046	1.043	1.030	1.015	0.990	0.968	0.949	0.932	0.869	0.795	0.695	0.623	0.427
35	1.042	1.039	1.027	1.014	0.991	0.970	0.952	0.936	0.875	0.804	0.703	0.631	0.433
40	1.038	1.035	1.025	1.012	0.991	0.971	0.954	0.939	0.881	0.811	0.711	0.638	0.438
45	1.034	1.031	1.022	1.010	0.990	0.972	0.956	0.942	0.886	0.817	0.718	0.645	0.443
50	1.030	1.028	1.019	1.008	0.989	0.972	0.957	0.943	0.889	0.822	0.724	0.651	0.447
55	1.027	1.024	1.016	1.006	0.988	0.972	0.957	0.944	0.892	0.826	0.729	0.656	0.451
60	1.023	1.021	1.013	1.004	0.986	0.971	0.957	0.944	0.894	0.829	0.733	0.660	0.454
65	1.020	1.018	1.010	1.001	0.985	0.970	0.956	0.944	0.895	0.832	0.735	0.664	0.457
70	1.017	1.015	1.007	0.999	0.983	0.968	0.955	0.943	0.896	0.834	0.739	0.667	0.459
75	1.014	1.012	1.005	0.996	0.981	0.967	0.954	0.943	0.896	0.835	0.741	0.669	0.461
80	1.011	1.009	1.002	0.994	0.979	0.965	0.953	0.941	0.895	0.835	0.742	0.670	0.462
85	1.008	1.006	0.999	0.991	0.976	0.963	0.951	0.940	0.895	0.835	0.743	0.671	0.463
90	1.005	1.003	0.996	0.988	0.974	0.961	0.949	0.938	0.893	0.834	0.743	0.671	0.463
95	1.002	0.999	0.993	0.986	0.971	0.958	0.947	0.936	0.892	0.833	0.742	0.670	0.463
100	0.999	0.997	0.991	0.983	0.969	0.956	0.944	0.933	0.889	0.831	0.740	0.669	0.462
105	0.996	0.994	0.988	0.980	0.966	0.953	0.941	0.930	0.887	0.829	0.738	0.667	0.461
110	0.993	0.991	0.985	0.977	0.963	0.950	0.938	0.927	0.884	0.826	0.735	0.665	0.459
115	0.990	0.988	0.982	0.974	0.960	0.947	0.935	0.924	0.880	0.822	0.732	0.662	0.457
120	0.987	0.985	0.979	0.971	0.956	0.943	0.931	0.920	0.876	0.818	0.728	0.658	0.454
125	0.984	0.982	0.975	0.967	0.953	0.940	0.928	0.916	0.872	0.813	0.723	0.653	0.451
130	0.981	0.979	0.972	0.964	0.949	0.935	0.923	0.912	0.867	0.808	0.718	0.648	0.447
135	0.978	0.976	0.969	0.960	0.945	0.931	0.919	0.907	0.862	0.802	0.712	0.642	0.443
140	0.974	0.973	0.965	0.957	0.941	0.927	0.914	0.902	0.855	0.795	0.705	0.635	0.438
145	0.971	0.969	0.961	0.953	0.936	0.921	0.908	0.896	0.848	0.788	0.697	0.628	0.432
150	0.968	0.966	0.958	0.948	0.931	0.915	0.902	0.890	0.841	0.779	0.688	0.620	0.426
155	0.964	0.962	0.953	0.943	0.925	0.910	0.895	0.882	0.832	0.770	0.679	0.611	0.420
160	0.960	0.958	0.949	0.938	0.919	0.903	0.888	0.874	0.823	0.760	0.669	0.601	0.413
165	0.982	0.971	0.959	0.951	0.912	0.895	0.879	0.865	0.812	0.748	0.657	0.591	0.406
170	1.037	1.033	1.019	1.002	0.954	0.911	0.877	0.855	0.800	0.736	0.645	0.579	0.398
175	1.095	1.090	1.075	1.055	0.997	0.948	0.911	0.881	0.792	0.722	0.632	0.567	0.389
180	1.155	1.150	1.133	1.110	1.040	0.983	0.942	0.910	0.815	0.728	0.626	0.558	0.380
$\varphi = -\pi/2$													
0	1.397	1.391	1.349	1.201	1.071	1.001	0.954	0.919	0.819	0.729	0.626	0.558	0.380
5	1.501	1.492	1.381	1.231	1.096	1.025	0.977	0.941	0.839	0.747	0.641	0.571	0.389
10	1.618	1.605	1.412	1.258	1.121	1.048	0.999	0.962	0.857	0.764	0.655	0.584	0.398
15	1.750	1.733	1.441	1.284	1.144	1.069	1.019	0.982	0.875	0.779	0.669	0.596	0.406
20	1.902	1.942	1.468	1.307	1.165	1.089	1.038	1.000	0.891	0.794	0.681	0.607	0.413
25	2.080	1.952	1.492	1.330	1.185	1.107	1.055	1.017	0.906	0.807	0.693	0.617	0.420
30	2.292	1.982	1.515	1.350	1.203	1.124	1.072	1.032	0.920	0.819	0.703	0.627	0.427
35	2.550	2.009	1.537	1.369	1.220	1.140	1.087	1.047	0.933	0.831	0.713	0.635	0.433
40	2.873	2.035	1.556	1.386	1.235	1.154	1.100	1.060	0.944	0.841	0.722	0.643	0.438
45	3.290	2.057	1.573	1.402	1.249	1.167	1.113	1.072	0.955	0.851	0.730	0.651	0.443
50	3.852	2.078	1.589	1.416	1.261	1.179	1.124	1.083	0.964	0.859	0.738	0.657	0.448
55	4.652	2.096	1.603	1.428	1.272	1.189	1.133	1.092	0.973	0.867	0.744	0.663	0.452
60	5.884	2.111	1.615	1.438	1.281	1.198	1.142	1.100	0.980	0.873	0.749	0.668	0.455
65	8.031	2.125	1.625	1.447	1.289	1.205	1.149	1.107	0.986	0.879	0.754	0.672	0.458
70		2.135	1.633	1.455	1.296	1.211	1.155	1.112	0.991	0.883	0.758	0.675	0.460
75		2.144	1.639	1.460	1.301	1.215	1.159	1.117	0.995	0.886	0.761	0.678	0.462
80		2.150	1.644	1.465	1.305	1.219	1.162	1.120	0.998	0.889	0.763	0.680	0.463
85		2.153	1.647	1.467	1.307	1.222	1.164	1.122	0.999	0.890	0.764	0.681	0.464
90	9.437	2.154	1.648	1.468	1.308	1.222	1.165	1.122	1.000	0.891	0.765	0.681	0.464
95	6.617	2.153	1.647	1.467	1.307	1.222	1.164	1.122	0.999	0.890	0.764	0.681	0.464
100	5.115	2.150	1.644	1.465	1.305	1.219	1.162	1.120	0.998	0.889	0.763	0.680	0.463
105	4.183	2.144	1.639	1.460	1.301	1.216	1.159	1.117	0.995	0.886	0.761	0.678	0.462
110	3.549	2.135	1.633	1.455	1.296	1.211	1.155	1.112	0.991	0.883	0.758	0.675	0.460
115	3.089	2.125	1.625	1.447	1.289	1.205	1.149	1.107	0.986	0.879	0.754	0.672	0.458
120	2.739	2.111	1.615	1.438	1.281	1.198	1.142	1.100	0.980	0.873	0.749	0.668	0.455
125	2.463	2.096	1.603	1.428	1.272	1.189	1.133	1.092	0.973	0.867	0.744	0.663	0.452
130	2.240	2.078	1.589	1.416	1.261	1.179	1.124	1.083	0.964	0.859	0.738	0.657	0.448
135	2.056	2.014	1.573	1.402	1.249	1.167	1.113	1.072	0.955	0.851	0.730	0.651	0.443
140	1.899	1.876	1.556	1.386	1.235	1.154	1.100	1.060	0.944	0.841	0.722	0.643	0.438
145	1.765	1.748	1.537	1.369	1.220	1.140	1.087	1.047	0.933	0.831	0.713	0.635	0.433
150	1.648	1.634	1.516	1.350	1.203	1.124	1.072	1.032	0.920	0.819	0.703	0.627	0.427
155	1.544	1.533	1.490	1.330	1.185	1.107	1.055	1.017	0.906	0.807	0.693	0.617	0.420
160	1.451	1.443	1.407	1.307	1.165	1.089	1.038	1.000	0.891	0.794	0.681	0.607	0.413
165	1.367	1.361	1.326	1.279	1.142	1.068	1.018	0.981	0.874	0.779	0.669	0.596	0.406
170	1.291	1.297	1.264	1.228	1.114	1.044	0.996	0.960	0.856	0.763	0.655	0.584	0.398
175	1.220	1.215	1.199	1.168	1.079	1.015	0.971	0.937	0.837	0.746	0.641	0.571	0.389
180	1.155	1.150	1.132	1.110	1.040	0.983	0.942	0.910	0.815	0.728	0.626	0.558	0.380

TABLE II. - COORDINATES θ AND ρ OF BOUNDARY OF HOLLOW IN THE MERIDIAN PLANE CONTAINING THE DIPOLE AXIS AND THE SUN-EARTH LINE FOR VARIOUS p_0/p_d - Continued
(d) $\lambda = 17.25$

θ , deg	p_0/p_d												
	0.	0.01	0.05	0.1	0.2	0.3	0.4	0.5	1.	2.	5.	10.	100.
	$\varphi = \pi/2$												
0	1.483	1.473	1.349	1.202	1.071	1.001	0.954	0.919	0.819	0.729	0.626	0.558	0.380
5	1.376	1.369	1.314	1.171	1.043	0.975	0.929	0.895	0.814	0.736	0.637	0.570	0.389
10	1.280	1.282	1.246	1.134	1.012	0.954	0.927	0.905	0.830	0.751	0.651	0.582	0.398
15	1.192	1.185	1.163	1.087	0.998	0.966	0.940	0.918	0.844	0.765	0.664	0.594	0.406
20	1.111	1.106	1.079	1.046	1.005	0.975	0.950	0.930	0.857	0.778	0.676	0.605	0.413
25	1.083	1.074	1.051	1.040	1.008	0.981	0.958	0.938	0.868	0.789	0.687	0.614	0.420
30	1.075	1.071	1.056	1.039	1.010	0.985	0.963	0.945	0.877	0.799	0.696	0.624	0.427
35	1.068	1.065	1.052	1.037	1.010	0.987	0.967	0.949	0.884	0.808	0.705	0.632	0.433
40	1.062	1.059	1.047	1.033	1.009	0.987	0.969	0.952	0.889	0.815	0.713	0.639	0.438
45	1.056	1.053	1.042	1.029	1.007	0.987	0.970	0.954	0.894	0.821	0.720	0.646	0.443
50	1.050	1.047	1.037	1.026	1.005	0.986	0.970	0.955	0.897	0.826	0.726	0.652	0.447
55	1.044	1.042	1.033	1.022	1.002	0.985	0.969	0.955	0.899	0.830	0.731	0.657	0.451
60	1.039	1.037	1.028	1.018	0.999	0.983	0.968	0.954	0.901	0.834	0.735	0.661	0.454
65	1.034	1.032	1.023	1.014	0.996	0.980	0.966	0.953	0.901	0.836	0.738	0.665	0.457
70	1.029	1.027	1.019	1.010	0.993	0.978	0.964	0.951	0.902	0.837	0.741	0.667	0.459
75	1.024	1.022	1.015	1.006	0.990	0.975	0.962	0.949	0.901	0.838	0.742	0.669	0.461
80	1.019	1.018	1.010	1.002	0.986	0.972	0.959	0.947	0.900	0.838	0.744	0.671	0.462
85	1.015	1.013	1.005	0.998	0.982	0.969	0.956	0.945	0.898	0.837	0.744	0.671	0.463
90	1.010	1.009	1.002	0.994	0.979	0.965	0.953	0.942	0.896	0.836	0.744	0.671	0.463
95	1.006	0.997	0.997	0.989	0.975	0.962	0.950	0.939	0.894	0.834	0.743	0.671	0.463
100	1.001	0.997	0.993	0.985	0.971	0.958	0.946	0.935	0.891	0.832	0.741	0.669	0.462
105	0.997	0.996	0.989	0.981	0.967	0.954	0.942	0.931	0.888	0.829	0.738	0.667	0.461
110	0.993	0.991	0.984	0.977	0.963	0.950	0.938	0.927	0.884	0.826	0.735	0.665	0.459
115	0.988	0.986	0.980	0.972	0.958	0.946	0.934	0.923	0.880	0.822	0.732	0.661	0.457
120	0.984	0.982	0.976	0.968	0.954	0.941	0.929	0.918	0.875	0.817	0.728	0.657	0.454
125	0.979	0.978	0.971	0.963	0.949	0.935	0.924	0.913	0.870	0.812	0.723	0.653	0.451
130	0.975	0.973	0.966	0.959	0.944	0.931	0.919	0.908	0.864	0.806	0.717	0.647	0.447
135	0.970	0.968	0.962	0.954	0.939	0.926	0.914	0.902	0.858	0.800	0.711	0.641	0.443
140	0.966	0.964	0.957	0.949	0.933	0.920	0.908	0.896	0.851	0.793	0.703	0.635	0.438
145	0.961	0.959	0.952	0.943	0.928	0.914	0.901	0.890	0.844	0.785	0.696	0.627	0.432
150	0.956	0.954	0.946	0.938	0.921	0.907	0.894	0.882	0.836	0.776	0.687	0.619	0.426
155	0.951	0.948	0.941	0.932	0.915	0.900	0.887	0.874	0.827	0.767	0.677	0.610	0.420
160	0.945	0.943	0.935	0.925	0.908	0.892	0.878	0.866	0.817	0.756	0.667	0.600	0.413
165	0.933	0.923	0.938	0.925	0.900	0.884	0.869	0.856	0.806	0.745	0.656	0.590	0.406
170	1.004	1.000	0.987	0.972	0.935	0.898	0.867	0.846	0.794	0.732	0.644	0.579	0.397
175	1.057	1.052	1.038	1.022	0.978	0.935	0.901	0.874	0.788	0.719	0.631	0.566	0.389
180	1.112	1.108	1.092	1.073	1.020	0.972	0.934	0.904	0.812	0.727	0.625	0.557	0.380
$\varphi = -\pi/2$													
0	1.483	1.473	1.349	1.202	1.071	1.001	0.954	0.919	0.819	0.729	0.626	0.558	0.380
5	1.602	1.589	1.381	1.231	1.096	1.025	0.977	0.941	0.839	0.747	0.641	0.571	0.389
10	1.737	1.720	1.412	1.258	1.121	1.048	0.999	0.962	0.857	0.764	0.655	0.584	0.398
15	1.894	1.870	1.441	1.284	1.144	1.069	1.019	0.982	0.875	0.779	0.669	0.596	0.406
20	2.077	1.919	1.468	1.307	1.165	1.089	1.038	1.000	0.891	0.794	0.681	0.607	0.413
25	2.295	1.952	1.492	1.330	1.185	1.107	1.055	1.017	0.906	0.807	0.693	0.617	0.420
30	2.562	1.982	1.515	1.350	1.203	1.124	1.072	1.032	0.920	0.819	0.703	0.627	0.427
35	2.896	2.009	1.537	1.369	1.220	1.140	1.087	1.047	0.933	0.831	0.713	0.635	0.433
40	3.331	2.035	1.556	1.386	1.235	1.154	1.100	1.060	0.944	0.841	0.722	0.643	0.438
45	3.919	2.057	1.573	1.402	1.249	1.167	1.113	1.072	0.955	0.851	0.730	0.651	0.443
50	4.765	2.078	1.589	1.416	1.261	1.179	1.124	1.083	0.964	0.859	0.738	0.657	0.448
55	6.086	2.096	1.603	1.428	1.272	1.189	1.133	1.092	0.973	0.867	0.744	0.663	0.452
60	8.445	2.111	1.615	1.438	1.281	1.198	1.142	1.100	0.980	0.873	0.749	0.668	0.455
65		2.125	1.625	1.447	1.289	1.205	1.149	1.107	0.986	0.879	0.754	0.672	0.458
70		2.135	1.633	1.455	1.296	1.211	1.155	1.112	0.991	0.883	0.758	0.675	0.460
75		2.144	1.639	1.460	1.301	1.215	1.159	1.117	0.995	0.886	0.761	0.678	0.462
80		2.150	1.644	1.465	1.305	1.219	1.162	1.120	0.998	0.889	0.763	0.680	0.463
85	8.823	2.153	1.647	1.467	1.307	1.222	1.164	1.122	0.999	0.890	0.764	0.681	0.464
90	6.309	2.154	1.648	1.468	1.308	1.222	1.165	1.122	1.000	0.891	0.765	0.681	0.464
95	4.931	2.153	1.647	1.467	1.307	1.222	1.164	1.122	0.999	0.890	0.764	0.681	0.464
100	4.063	2.150	1.644	1.465	1.305	1.219	1.162	1.120	0.998	0.889	0.763	0.680	0.463
105	3.465	2.144	1.639	1.460	1.301	1.216	1.159	1.117	0.995	0.886	0.761	0.678	0.462
110	3.029	2.135	1.633	1.455	1.296	1.211	1.155	1.112	0.991	0.883	0.758	0.675	0.460
115	2.696	2.125	1.625	1.447	1.289	1.205	1.149	1.107	0.986	0.879	0.754	0.672	0.458
120	2.433	2.111	1.615	1.438	1.281	1.198	1.142	1.100	0.980	0.873	0.749	0.668	0.455
125	2.219	2.096	1.603	1.428	1.272	1.189	1.133	1.092	0.973	0.867	0.744	0.663	0.452
130	2.041	2.006	1.589	1.416	1.261	1.179	1.124	1.083	0.964	0.859	0.738	0.657	0.448
135	1.890	1.864	1.573	1.402	1.249	1.167	1.113	1.072	0.955	0.851	0.730	0.651	0.443
140	1.761	1.739	1.556	1.386	1.235	1.154	1.100	1.060	0.944	0.841	0.722	0.643	0.438
145	1.648	1.630	1.541	1.369	1.220	1.140	1.087	1.047	0.933	0.831	0.713	0.635	0.433
150	1.547	1.531	1.493	1.350	1.203	1.124	1.072	1.032	0.920	0.819	0.703	0.627	0.427
155	1.457	1.442	1.413	1.330	1.185	1.107	1.055	1.017	0.906	0.807	0.693	0.617	0.420
160	1.377	1.359	1.340	1.302	1.163	1.088	1.037	0.999	0.891	0.794	0.681	0.607	0.413
165	1.302	1.289	1.270	1.245	1.136	1.065	1.016	0.980	0.874	0.779	0.669	0.596	0.406
170	1.234	1.226	1.208	1.183	1.102	1.038	0.992	0.957	0.855	0.763	0.655	0.584	0.398
175	1.171	1.166	1.148	1.127	1.063	1.006	0.964	0.932	0.835	0.745	0.641	0.571	0.389
180	1.112	1.107	1.092	1.073	1.020	0.972	0.934	0.904	0.812	0.727	0.625	0.557	0.380

TABLE II.- COORDINATES θ AND ρ OF BOUNDARY OF HOLLOW IN THE MERIDIAN PLANE CONTAINING THE DIPOLE AXIS AND THE SUN-EARTH LINE FOR VARIOUS p_o/p_d - Continued
(e) $\lambda = 23.00$

θ , deg	p_o/p_d												
	0.	0.01	0.05	0.1	0.2	0.3	0.4	0.5	1.	2.	5.	10.	100.
$\varphi = \pi/2$													
0	1.583	1.569	1.349	1.202	1.071	1.001	0.954	0.919	0.819	0.729	0.626	0.558	0.380
5	1.461	1.450	1.314	1.171	1.043	0.975	0.929	0.898	0.819	0.738	0.638	0.570	0.389
10	1.352	1.344	1.276	1.138	1.014	0.968	0.939	0.914	0.835	0.754	0.652	0.582	0.398
15	1.253	1.248	1.214	1.099	1.017	0.981	0.952	0.929	0.850	0.768	0.665	0.594	0.406
20	1.164	1.157	1.134	1.075	1.025	0.991	0.964	0.941	0.863	0.781	0.677	0.605	0.413
25	1.121	1.115	1.081	1.066	1.030	0.999	0.973	0.951	0.875	0.793	0.688	0.615	0.420
30	1.110	1.105	1.087	1.066	1.032	1.003	0.979	0.958	0.884	0.803	0.698	0.624	0.427
35	1.100	1.095	1.080	1.062	1.031	1.005	0.983	0.963	0.892	0.812	0.707	0.633	0.433
40	1.090	1.087	1.073	1.057	1.029	1.005	0.984	0.966	0.898	0.820	0.715	0.643	0.438
45	1.081	1.078	1.066	1.052	1.026	1.004	0.985	0.967	0.903	0.826	0.722	0.647	0.443
50	1.073	1.070	1.059	1.046	1.023	1.002	0.984	0.968	0.906	0.831	0.728	0.653	0.447
55	1.065	1.063	1.052	1.040	1.019	0.999	0.982	0.967	0.908	0.835	0.733	0.658	0.451
60	1.058	1.055	1.046	1.035	1.014	0.995	0.980	0.966	0.909	0.838	0.737	0.662	0.454
65	1.051	1.048	1.039	1.029	1.010	0.993	0.977	0.964	0.909	0.840	0.740	0.666	0.457
70	1.044	1.042	1.033	1.023	1.005	0.989	0.974	0.961	0.908	0.842	0.743	0.668	0.460
75	1.037	1.035	1.027	1.018	1.000	0.985	0.971	0.958	0.907	0.842	0.744	0.670	0.461
80	1.031	1.029	1.021	1.012	0.996	0.981	0.967	0.955	0.905	0.842	0.745	0.672	0.463
85	1.024	1.023	1.015	1.007	0.991	0.976	0.963	0.951	0.903	0.841	0.745	0.672	0.463
90	1.018	1.017	1.009	1.001	0.986	0.972	0.959	0.947	0.900	0.839	0.745	0.672	0.463
95	1.012	1.011	1.003	0.996	0.981	0.967	0.955	0.943	0.897	0.837	0.744	0.671	0.463
100	1.006	1.007	0.997	0.990	0.975	0.962	0.950	0.939	0.893	0.834	0.742	0.670	0.462
105	1.000	0.998	0.992	0.984	0.970	0.957	0.945	0.934	0.889	0.831	0.739	0.668	0.461
110	0.994	0.993	0.986	0.979	0.964	0.951	0.940	0.929	0.885	0.827	0.736	0.665	0.459
115	0.989	0.987	0.981	0.973	0.959	0.946	0.934	0.923	0.880	0.822	0.732	0.661	0.457
120	0.983	0.981	0.975	0.967	0.953	0.940	0.929	0.918	0.875	0.817	0.727	0.657	0.454
125	0.977	0.975	0.969	0.961	0.947	0.934	0.923	0.912	0.869	0.811	0.722	0.653	0.451
130	0.971	0.969	0.963	0.955	0.941	0.928	0.916	0.906	0.862	0.805	0.716	0.647	0.447
135	0.965	0.963	0.957	0.949	0.935	0.922	0.910	0.899	0.856	0.798	0.710	0.641	0.443
140	0.959	0.957	0.950	0.943	0.928	0.915	0.903	0.892	0.848	0.791	0.703	0.634	0.438
145	0.953	0.951	0.944	0.936	0.921	0.908	0.896	0.885	0.840	0.783	0.695	0.627	0.432
150	0.946	0.944	0.937	0.929	0.914	0.900	0.888	0.877	0.832	0.774	0.686	0.619	0.426
155	0.940	0.938	0.930	0.922	0.906	0.892	0.879	0.868	0.822	0.764	0.676	0.610	0.420
160	0.933	0.931	0.923	0.914	0.898	0.884	0.870	0.859	0.812	0.753	0.665	0.600	0.413
165	0.926	0.923	0.924	0.915	0.889	0.874	0.861	0.849	0.801	0.742	0.655	0.589	0.405
170	0.974	0.970	0.955	0.943	0.915	0.884	0.857	0.838	0.789	0.729	0.643	0.578	0.397
175	1.023	1.018	1.006	0.992	0.957	0.921	0.891	0.866	0.785	0.716	0.630	0.566	0.389
180	1.073	1.069	1.056	1.039	0.999	0.957	0.924	0.896	0.809	0.725	0.625	0.557	0.380
$\varphi = -\pi/2$													
0	1.583	1.569	1.349	1.202	1.071	1.001	0.954	0.919	0.819	0.729	0.626	0.558	0.380
5	1.721	1.704	1.381	1.231	1.096	1.025	0.977	0.941	0.839	0.747	0.641	0.571	0.389
10	1.881	1.847	1.412	1.258	1.121	1.048	0.999	0.962	0.857	0.764	0.655	0.584	0.398
15	2.069	1.884	1.441	1.284	1.144	1.069	1.019	0.982	0.875	0.779	0.669	0.596	0.406
20	2.294	1.919	1.468	1.307	1.165	1.089	1.038	1.000	0.891	0.794	0.681	0.607	0.413
25	2.569	1.952	1.492	1.330	1.185	1.107	1.055	1.017	0.906	0.807	0.693	0.617	0.420
30	2.915	1.982	1.515	1.350	1.203	1.124	1.072	1.032	0.920	0.819	0.703	0.627	0.427
35	3.366	2.009	1.537	1.369	1.220	1.140	1.087	1.047	0.933	0.831	0.713	0.635	0.433
40	3.982	2.035	1.556	1.386	1.235	1.154	1.100	1.060	0.944	0.841	0.722	0.643	0.438
45	4.875	2.057	1.573	1.402	1.249	1.167	1.113	1.072	0.955	0.851	0.730	0.651	0.443
50	6.293	2.078	1.589	1.416	1.261	1.179	1.124	1.083	0.964	0.859	0.738	0.657	0.448
55	8.892	2.096	1.603	1.428	1.272	1.189	1.133	1.092	0.973	0.867	0.744	0.663	0.452
60		2.111	1.615	1.438	1.281	1.198	1.142	1.100	0.980	0.873	0.749	0.668	0.455
65		2.125	1.625	1.447	1.289	1.205	1.149	1.107	0.986	0.879	0.754	0.672	0.458
70		2.135	1.633	1.455	1.296	1.211	1.155	1.112	0.991	0.883	0.758	0.675	0.460
75		2.144	1.639	1.460	1.301	1.216	1.159	1.117	0.995	0.886	0.761	0.678	0.462
80	8.262	2.150	1.644	1.465	1.305	1.219	1.162	1.120	0.998	0.889	0.763	0.680	0.463
85	6.014	2.153	1.647	1.467	1.307	1.222	1.164	1.122	0.999	0.890	0.764	0.681	0.464
90	4.750	2.154	1.648	1.468	1.308	1.222	1.165	1.122	1.000	0.891	0.765	0.681	0.464
95	3.942	2.153	1.647	1.467	1.307	1.222	1.164	1.122	0.999	0.890	0.764	0.681	0.464
100	3.380	2.150	1.644	1.465	1.305	1.219	1.162	1.120	0.998	0.889	0.763	0.680	0.463
105	2.967	2.144	1.639	1.460	1.301	1.216	1.159	1.117	0.995	0.886	0.761	0.678	0.462
110	2.650	2.135	1.633	1.455	1.296	1.211	1.155	1.112	0.991	0.883	0.758	0.675	0.460
115	2.399	2.125	1.625	1.447	1.289	1.205	1.149	1.107	0.986	0.879	0.754	0.672	0.458
120	2.194	2.111	1.615	1.438	1.281	1.198	1.142	1.100	0.980	0.873	0.749	0.668	0.455
125	2.023	1.993	1.603	1.428	1.272	1.189	1.133	1.092	0.973	0.867	0.744	0.663	0.452
130	1.879	1.856	1.589	1.416	1.261	1.179	1.124	1.083	0.964	0.859	0.738	0.657	0.448
135	1.754	1.737	1.573	1.402	1.249	1.167	1.113	1.072	0.955	0.851	0.730	0.651	0.443
140	1.645	1.632	1.563	1.386	1.235	1.154	1.100	1.060	0.944	0.841	0.722	0.643	0.438
145	1.548	1.538	1.495	1.369	1.220	1.140	1.087	1.047	0.933	0.831	0.713	0.635	0.433
150	1.462	1.453	1.418	1.350	1.203	1.124	1.072	1.032	0.920	0.819	0.703	0.627	0.427
155	1.383	1.376	1.347	1.312	1.183	1.106	1.055	1.016	0.906	0.807	0.693	0.617	0.420
160	1.312	1.307	1.279	1.256	1.157	1.085	1.035	0.998	0.890	0.793	0.681	0.607	0.413
165	1.246	1.247	1.220	1.196	1.123	1.058	1.012	0.976	0.872	0.778	0.668	0.595	0.406
170	1.184	1.176	1.162	1.141	1.083	1.027	0.985	0.952	0.853	0.762	0.655	0.584	0.398
175	1.127	1.121	1.107	1.089	1.041	0.993	0.955	0.925	0.832	0.744	0.640	0.571	0.389
180	1.073	1.069	1.056	1.039	0.999	0.957	0.924	0.896	0.809	0.725	0.625	0.557	0.380

TABLE II.- COORDINATES θ AND ρ OF BOUNDARY OF HOLLOW IN THE MERIDIAN PLANE CONTAINING THE DIPOLE AXIS AND THE SUN-EARTH LINE FOR VARIOUS p_0/p_d - Continued
(f) $\lambda = 28.75$

θ , deg	p_0/p_d												
	0.	0.01	0.05	0.1	0.2	0.3	0.4	0.5	1.	2.	5.	10.	100.
	$\varphi = \pi/2$												
0	1.701	1.691	1.349	1.202	1.071	1.001	0.954	0.919	0.819	0.729	0.626	0.558	0.380
5	1.559	1.545	1.314	1.171	1.043	0.975	0.932	0.906	0.823	0.740	0.639	0.570	0.389
10	1.435	1.424	1.278	1.138	1.022	0.981	0.949	0.923	0.840	0.756	0.653	0.583	0.398
15	1.324	1.315	1.237	1.104	1.035	0.995	0.964	0.938	0.855	0.771	0.665	0.595	0.406
20	1.223	1.149	1.176	1.095	1.045	1.007	0.976	0.952	0.869	0.784	0.678	0.605	0.413
25	1.165	1.157	1.128	1.098	1.052	1.016	0.987	0.962	0.881	0.796	0.689	0.616	0.420
30	1.150	1.144	1.121	1.096	1.055	1.022	0.994	0.971	0.891	0.807	0.699	0.625	0.427
35	1.136	1.131	1.112	1.091	1.054	1.024	0.999	0.977	0.900	0.817	0.708	0.633	0.433
40	1.123	1.119	1.103	1.084	1.052	1.025	1.001	0.981	0.907	0.825	0.717	0.641	0.438
45	1.112	1.108	1.094	1.077	1.048	1.023	1.001	0.982	0.912	0.831	0.724	0.648	0.443
50	1.100	1.097	1.084	1.070	1.043	1.020	1.000	0.982	0.915	0.836	0.730	0.654	0.447
55	1.090	1.087	1.075	1.062	1.038	1.016	0.998	0.981	0.917	0.841	0.735	0.659	0.451
60	1.080	1.077	1.067	1.054	1.032	1.012	0.994	0.979	0.918	0.843	0.739	0.663	0.455
65	1.071	1.068	1.058	1.047	1.026	1.007	0.991	0.976	0.917	0.845	0.742	0.667	0.457
70	1.062	1.059	1.050	1.039	1.020	1.002	0.987	0.972	0.916	0.846	0.745	0.669	0.460
75	1.053	1.051	1.042	1.032	1.014	0.997	0.982	0.968	0.915	0.846	0.745	0.671	0.461
80	1.045	1.043	1.035	1.025	1.007	0.991	0.977	0.964	0.912	0.846	0.747	0.673	0.463
85	1.037	1.035	1.027	1.018	1.001	0.986	0.972	0.959	0.909	0.844	0.747	0.673	0.463
90	1.029	1.027	1.019	1.011	0.994	0.980	0.967	0.954	0.906	0.842	0.746	0.673	0.464
95	1.021	1.019	1.012	1.003	0.989	0.976	0.962	0.950	0.902	0.840	0.745	0.672	0.463
100	1.014	1.012	1.005	0.995	0.981	0.968	0.955	0.944	0.897	0.836	0.743	0.670	0.462
105	1.006	1.004	0.998	0.990	0.975	0.961	0.949	0.938	0.892	0.833	0.740	0.668	0.461
110	0.999	0.997	0.990	0.983	0.968	0.955	0.943	0.932	0.887	0.828	0.737	0.665	0.459
115	0.991	0.990	0.983	0.975	0.961	0.948	0.936	0.925	0.881	0.823	0.732	0.662	0.457
120	0.984	0.982	0.975	0.968	0.954	0.941	0.930	0.919	0.875	0.818	0.728	0.658	0.454
125	0.977	0.975	0.969	0.961	0.947	0.934	0.923	0.912	0.869	0.811	0.722	0.653	0.451
130	0.969	0.968	0.961	0.954	0.940	0.927	0.915	0.905	0.862	0.805	0.716	0.647	0.447
135	0.962	0.960	0.954	0.946	0.932	0.920	0.908	0.897	0.854	0.797	0.709	0.641	0.443
140	0.955	0.953	0.946	0.939	0.925	0.912	0.900	0.889	0.846	0.789	0.702	0.634	0.438
145	0.947	0.945	0.939	0.931	0.916	0.904	0.892	0.881	0.838	0.781	0.694	0.626	0.432
150	0.939	0.937	0.931	0.923	0.908	0.895	0.883	0.872	0.828	0.772	0.685	0.618	0.426
155	0.931	0.929	0.922	0.914	0.899	0.886	0.874	0.863	0.819	0.762	0.675	0.609	0.420
160	0.923	0.921	0.914	0.906	0.890	0.876	0.864	0.853	0.808	0.751	0.665	0.599	0.413
165	0.914	0.914	0.906	0.899	0.880	0.866	0.854	0.842	0.797	0.739	0.654	0.589	0.405
170	0.948	0.943	0.928	0.920	0.896	0.869	0.845	0.831	0.784	0.726	0.641	0.577	0.397
175	0.985	0.989	0.978	0.964	0.936	0.906	0.879	0.856	0.780	0.713	0.628	0.565	0.389
180	1.039	1.036	1.023	1.008	0.976	0.942	0.912	0.887	0.805	0.723	0.624	0.557	0.380
$\varphi = -\pi/2$													
0	1.701	1.691	1.349	1.202	1.071	1.001	0.954	0.919	0.819	0.729	0.626	0.558	0.380
5	1.865	1.807	1.381	1.231	1.096	1.025	0.977	0.941	0.839	0.747	0.641	0.571	0.389
10	2.057	1.847	1.412	1.258	1.121	1.048	0.999	0.962	0.857	0.764	0.655	0.584	0.398
15	2.288	1.884	1.441	1.284	1.144	1.069	1.019	0.982	0.875	0.779	0.669	0.596	0.406
20	2.570	1.919	1.468	1.307	1.165	1.089	1.038	1.000	0.891	0.794	0.681	0.607	0.413
25	2.928	1.952	1.492	1.330	1.185	1.107	1.055	1.017	0.906	0.807	0.693	0.617	0.420
30	3.396	1.982	1.515	1.350	1.203	1.124	1.072	1.032	0.920	0.819	0.703	0.627	0.427
35	4.040	2.009	1.537	1.369	1.220	1.140	1.087	1.047	0.933	0.831	0.713	0.635	0.433
40	4.983	2.035	1.556	1.386	1.235	1.154	1.100	1.060	0.944	0.841	0.722	0.643	0.438
45	6.505	2.057	1.573	1.402	1.249	1.167	1.113	1.072	0.955	0.851	0.730	0.651	0.443
50	9.379	2.078	1.589	1.416	1.261	1.179	1.124	1.083	0.964	0.859	0.738	0.657	0.448
55		2.096	1.603	1.428	1.272	1.189	1.133	1.092	0.973	0.867	0.744	0.663	0.452
60		2.111	1.615	1.438	1.281	1.198	1.142	1.100	0.980	0.873	0.749	0.668	0.455
65		2.125	1.625	1.447	1.289	1.205	1.149	1.107	0.986	0.879	0.754	0.672	0.458
70		2.135	1.633	1.455	1.296	1.211	1.155	1.112	0.991	0.883	0.758	0.675	0.460
75	7.747	2.144	1.639	1.460	1.301	1.216	1.159	1.117	0.995	0.886	0.761	0.678	0.462
80	5.731	2.150	1.644	1.465	1.305	1.219	1.162	1.120	0.998	0.889	0.763	0.680	0.463
85	4.571	2.153	1.647	1.467	1.307	1.222	1.164	1.122	0.999	0.890	0.764	0.681	0.464
90	3.819	2.154	1.648	1.468	1.308	1.222	1.165	1.122	1.000	0.891	0.765	0.681	0.464
95	3.292	2.153	1.647	1.467	1.307	1.222	1.164	1.122	0.999	0.890	0.764	0.681	0.464
100	2.902	2.150	1.644	1.465	1.305	1.219	1.162	1.120	0.998	0.889	0.763	0.680	0.463
105	2.601	2.144	1.639	1.460	1.301	1.215	1.159	1.117	0.995	0.886	0.761	0.678	0.462
110	2.362	2.135	1.633	1.455	1.296	1.211	1.155	1.112	0.991	0.883	0.758	0.675	0.460
115	2.166	2.123	1.625	1.447	1.289	1.205	1.149	1.107	0.986	0.879	0.754	0.672	0.458
120	2.003	1.973	1.615	1.438	1.281	1.198	1.142	1.100	0.980	0.873	0.749	0.668	0.455
125	1.864	1.842	1.603	1.428	1.272	1.189	1.133	1.092	0.973	0.867	0.744	0.663	0.452
130	1.744	1.727	1.589	1.416	1.261	1.179	1.124	1.083	0.964	0.859	0.738	0.657	0.448
135	1.639	1.626	1.573	1.402	1.249	1.167	1.113	1.072	0.955	0.851	0.730	0.651	0.443
140	1.546	1.536	1.494	1.386	1.235	1.154	1.100	1.060	0.944	0.841	0.722	0.643	0.438
145	1.463	1.454	1.419	1.374	1.220	1.140	1.087	1.047	0.933	0.831	0.713	0.635	0.433
150	1.388	1.380	1.351	1.317	1.201	1.123	1.071	1.032	0.920	0.819	0.703	0.627	0.427
155	1.319	1.312	1.286	1.256	1.176	1.103	1.052	1.015	0.905	0.807	0.693	0.617	0.420
160	1.255	1.247	1.228	1.203	1.141	1.077	1.030	0.994	0.888	0.793	0.681	0.607	0.413
165	1.196	1.191	1.173	1.151	1.101	1.045	1.004	0.971	0.870	0.777	0.668	0.595	0.406
170	1.141	1.136	1.121	1.101	1.059	1.013	0.975	0.945	0.850	0.760	0.654	0.583	0.398
175	1.089	1.085	1.071	1.054	1.018	0.978	0.945	0.916	0.828	0.742	0.640	0.571	0.389
180	1.039	1.036	1.023	1.008	0.976	0.942	0.912	0.887	0.805	0.723	0.624	0.557	0.380

TABLE II.- COORDINATES θ AND ρ OF BOUNDARY OF HOLLOW IN THE MERIDIAN PLANE CONTAINING THE DIPOLE AXIS AND THE SUN-EARTH LINE FOR VARIOUS p_0/p_d - Concluded
(g) $\lambda = 34.50$

θ , deg	P_0/P_d												
	0.	0.01	0.05	0.1	0.2	0.3	0.4	0.5	1.	2.	5.	10.	100.
	$\varphi = \pi/2$												
0	1.844	1.764	1.349	1.202	1.071	1.001	0.954	0.919	0.819	0.729	0.626	0.558	0.380
5	1.677	1.683	0.314	1.171	1.043	0.976	0.941	0.913	0.826	0.742	0.640	0.571	0.389
10	1.532	1.518	1.257	1.138	1.039	0.993	0.959	0.931	0.844	0.758	0.654	0.583	0.398
15	1.405	1.394	1.239	1.120	1.053	1.009	0.975	0.947	0.859	0.773	0.667	0.595	0.406
20	1.292	1.283	1.195	1.122	1.064	1.021	0.988	0.961	0.874	0.786	0.679	0.606	0.413
25	1.218	1.191	1.169	1.128	1.073	1.032	1.000	0.973	0.887	0.799	0.690	0.616	0.420
30	1.198	1.191	1.157	1.128	1.078	1.039	1.009	0.983	0.898	0.810	0.700	0.625	0.427
35	1.179	1.173	1.149	1.123	1.079	1.044	1.015	0.991	0.907	0.820	0.710	0.634	0.433
40	1.162	1.157	1.137	1.115	1.077	1.045	1.018	0.995	0.915	0.829	0.718	0.642	0.438
45	1.147	1.142	1.126	1.106	1.072	1.043	1.019	0.997	0.921	0.836	0.725	0.648	0.443
50	1.132	1.129	1.114	1.097	1.066	1.040	1.017	0.997	0.924	0.841	0.732	0.654	0.447
55	1.119	1.116	1.102	1.087	1.059	1.035	1.014	0.996	0.926	0.846	0.737	0.660	0.451
60	1.106	1.103	1.091	1.077	1.052	1.030	1.011	0.993	0.927	0.849	0.741	0.664	0.455
65	1.094	1.092	1.081	1.068	1.045	1.024	1.006	0.990	0.927	0.851	0.744	0.668	0.457
70	1.083	1.080	1.070	1.058	1.037	1.018	1.001	0.985	0.925	0.852	0.747	0.670	0.460
75	1.072	1.070	1.060	1.049	1.029	1.011	0.995	0.980	0.923	0.852	0.748	0.672	0.461
80	1.062	1.060	1.051	1.040	1.021	1.004	0.989	0.975	0.920	0.851	0.749	0.674	0.463
85	1.052	1.050	1.041	1.031	1.013	0.997	0.983	0.969	0.916	0.849	0.749	0.674	0.463
90	1.042	1.040	1.032	1.023	1.005	0.990	0.976	0.963	0.912	0.847	0.748	0.674	0.463
95	1.033	1.031	1.023	1.014	1.004	0.985	0.973	0.960	0.908	0.843	0.747	0.673	0.463
100	1.023	1.021	1.014	1.005	0.990	0.975	0.962	0.950	0.902	0.840	0.744	0.671	0.463
105	1.014	1.012	1.005	0.997	0.982	0.968	0.955	0.943	0.897	0.835	0.741	0.669	0.461
110	1.005	1.003	0.997	0.989	0.974	0.960	0.948	0.936	0.891	0.830	0.738	0.665	0.459
115	0.996	0.995	0.988	0.980	0.965	0.952	0.940	0.929	0.884	0.825	0.733	0.662	0.457
120	0.988	0.986	0.979	0.972	0.957	0.944	0.932	0.921	0.877	0.819	0.728	0.658	0.454
125	0.979	0.977	0.971	0.963	0.949	0.936	0.924	0.913	0.870	0.812	0.723	0.653	0.451
130	0.970	0.968	0.962	0.954	0.940	0.928	0.916	0.905	0.862	0.805	0.716	0.647	0.447
135	0.961	0.960	0.953	0.946	0.932	0.919	0.907	0.897	0.854	0.797	0.709	0.641	0.443
140	0.952	0.951	0.944	0.937	0.923	0.910	0.899	0.888	0.845	0.789	0.702	0.634	0.438
145	0.943	0.942	0.935	0.928	0.914	0.901	0.889	0.879	0.836	0.780	0.693	0.626	0.432
150	0.934	0.933	0.926	0.918	0.904	0.891	0.880	0.869	0.826	0.770	0.684	0.618	0.426
155	0.925	0.923	0.917	0.909	0.894	0.881	0.870	0.859	0.816	0.760	0.675	0.609	0.420
160	0.915	0.914	0.907	0.899	0.884	0.871	0.859	0.848	0.805	0.749	0.664	0.599	0.413
165	0.905	0.904	0.897	0.888	0.873	0.860	0.848	0.837	0.793	0.737	0.653	0.588	0.405
170	0.924	0.891	0.911	0.897	0.878	0.855	0.836	0.825	0.780	0.724	0.640	0.577	0.397
175	0.966	0.963	0.952	0.940	0.916	0.890	0.867	0.846	0.775	0.710	0.627	0.565	0.389
180	1.009	1.006	0.995	0.981	0.954	0.925	0.899	0.877	0.800	0.721	0.623	0.556	0.380

$\varphi = -\pi/2$													
0	1.844	1.764	1.349	1.202	1.071	1.001	0.954	0.919	0.819	0.729	0.625	0.558	0.380
5	2.041	1.807	1.381	1.231	1.096	1.025	0.977	0.941	0.839	0.747	0.641	0.571	0.389
10	2.277	1.847	1.412	1.258	1.121	1.048	0.999	0.962	0.857	0.764	0.655	0.584	0.398
15	2.567	1.884	1.441	1.284	1.144	1.069	1.019	0.982	0.875	0.779	0.669	0.596	0.406
20	2.936	1.919	1.468	1.307	1.165	1.089	1.038	1.000	0.891	0.794	0.681	0.607	0.413
25	3.421	1.952	1.492	1.330	1.185	1.107	1.055	1.017	0.906	0.807	0.693	0.617	0.420
30	4.093	1.982	1.515	1.350	1.203	1.124	1.072	1.032	0.920	0.819	0.703	0.627	0.427
35	5.089	2.009	1.537	1.369	1.220	1.140	1.087	1.047	0.933	0.831	0.713	0.635	0.433
40	6.724	2.035	1.556	1.386	1.235	1.154	1.100	1.060	0.944	0.841	0.722	0.643	0.438
45	9.913	2.057	1.573	1.402	1.249	1.167	1.113	1.072	0.955	0.851	0.730	0.651	0.443
50		2.078	1.589	1.416	1.261	1.179	1.124	1.083	0.964	0.859	0.738	0.657	0.448
55		2.096	1.603	1.428	1.272	1.189	1.133	1.092	0.973	0.867	0.744	0.663	0.452
60		2.111	1.615	1.438	1.281	1.198	1.142	1.100	0.980	0.873	0.749	0.668	0.455
65		2.125	1.625	1.447	1.289	1.205	1.149	1.107	0.986	0.879	0.754	0.672	0.458
70	7.260	2.135	1.633	1.455	1.296	1.211	1.155	1.112	0.991	0.883	0.758	0.675	0.460
75	5.460	2.144	1.639	1.460	1.301	1.216	1.159	1.117	0.995	0.886	0.761	0.678	0.462
80	4.395	2.150	1.644	1.465	1.305	1.219	1.162	1.120	0.998	0.889	0.763	0.680	0.463
85	3.696	2.153	1.647	1.467	1.307	1.222	1.164	1.122	0.999	0.890	0.764	0.681	0.464
90	3.202	2.154	1.648	1.468	1.308	1.222	1.165	1.122	1.000	0.891	0.765	0.681	0.464
95	2.834	2.153	1.647	1.467	1.307	1.222	1.164	1.122	0.999	0.890	0.764	0.681	0.464
100	2.550	2.150	1.644	1.465	1.305	1.219	1.162	1.120	0.998	0.889	0.763	0.680	0.463
105	2.322	2.144	1.639	1.460	1.301	1.216	1.159	1.117	0.995	0.886	0.761	0.678	0.462
110	2.136	2.094	1.633	1.455	1.296	1.211	1.155	1.112	0.991	0.883	0.758	0.675	0.460
115	1.980	1.951	1.625	1.447	1.289	1.205	1.149	1.107	0.986	0.879	0.754	0.672	0.458
120	1.847	1.826	1.615	1.438	1.281	1.198	1.142	1.100	0.980	0.873	0.749	0.668	0.455
125	1.732	1.716	1.603	1.428	1.272	1.189	1.133	1.092	0.973	0.867	0.744	0.663	0.452
130	1.632	1.619	1.568	1.416	1.261	1.179	1.124	1.083	0.964	0.859	0.738	0.657	0.448
135	1.542	1.532	1.491	1.402	1.249	1.167	1.113	1.072	0.955	0.851	0.730	0.651	0.443
140	1.462	1.453	1.420	1.376	1.235	1.154	1.100	1.050	0.944	0.841	0.722	0.643	0.438
145	1.390	1.382	1.354	1.320	1.218	1.139	1.086	1.046	0.932	0.831	0.713	0.635	0.433
150	1.323	1.317	1.295	1.261	1.193	1.119	1.068	1.030	0.919	0.819	0.703	0.627	0.427
155	1.262	1.255	1.235	1.211	1.157	1.094	1.047	1.011	0.903	0.806	0.692	0.617	0.420
160	1.205	1.205	1.182	1.161	1.116	1.064	1.021	0.988	0.886	0.792	0.681	0.607	0.413
165	1.152	1.149	1.132	1.113	1.075	1.030	0.993	0.963	0.867	0.776	0.668	0.595	0.406
170	1.102	1.099	1.084	1.067	1.034	0.996	0.963	0.935	0.846	0.759	0.654	0.583	0.398
175	1.054	1.051	1.038	1.023	0.994	0.961	0.931	0.906	0.823	0.740	0.639	0.570	0.389
180	1.009	1.006	0.995	0.981	0.954	0.925	0.899	0.877	0.800	0.721	0.623	0.556	0.380

TABLE III.- COORDINATES θ AND ρ OF NEUTRAL POINTS FOR VARIOUS λ AND p_o/p_d

λ , deg	p_o/p_d	Upper		Lower	
		θ , deg	ρ	θ , deg	ρ
0.	0.	19.10	1.000	160.90	1.000
	0.01	19.01	0.996	160.99	0.996
	0.05	18.90	0.983	161.10	0.983
	0.10	18.37	0.971	161.63	0.971
	0.20	15.14	0.943	164.86	0.943
	0.30	12.24	0.916	167.77	0.916
	0.40	10.10	0.892	169.90	0.892
	0.50	8.54	0.871	171.48	0.871
	1.00	4.73	0.797	175.30	0.797
	2.00	2.47	0.720	177.57	0.720
	5.00	1.00	0.623	179.02	0.623
	10.00	0.50	0.556	179.51	0.556
	100.00	0.05	0.380	179.95	0.380
5.75	0.	20.10	1.025	161.73	0.977
	0.01	20.00	1.022	161.91	0.973
	0.05	19.90	1.005	162.02	0.945
	0.10	18.95	0.992	162.42	0.952
	0.20	14.81	0.960	164.90	0.927
	0.30	11.54	0.929	167.39	0.903
	0.40	9.33	0.902	169.35	0.882
	0.50	7.80	0.879	170.86	0.863
	1.00	4.18	0.801	174.78	0.793
	2.00	2.11	0.722	177.24	0.718
	5.00	0.84	0.624	178.87	0.622
	10.00	0.42	0.557	179.43	0.556
	100.00	0.04	0.378	179.94	0.380
11.50	0.	20.67	1.055	162.82	0.958
	0.01	20.50	1.048	163.00	0.954
	0.05	20.20	1.033	163.10	0.945
	0.10	19.25	1.016	163.35	0.935
	0.20	14.06	0.978	165.23	0.912
	0.30	10.62	0.942	167.33	0.891
	0.40	8.39	0.912	169.08	0.871
	0.50	6.85	0.886	170.48	0.854
	1.00	3.50	0.834	174.35	0.789
	2.00	1.74	0.723	176.95	0.716
	5.00	0.69	0.623	178.73	0.622
	10.00	0.34	0.557	179.36	0.556
	100.00	0.03	0.380	179.94	0.380
17.25	0.	21.53	1.091	163.85	0.940
	0.01	21.43	1.084	163.90	0.936
	0.05	21.23	1.063	164.08	0.929
	0.10	19.01	1.045	164.24	0.915
	0.20	12.99	0.994	165.77	0.899
	0.30	9.21	0.952	167.54	0.879
	0.40	7.06	0.919	169.07	0.861
	0.50	5.71	0.892	170.33	0.845
	1.00	2.87	0.807	174.05	0.784
	2.00	1.41	0.724	176.71	0.714
	5.00	0.55	0.624	178.61	0.621
	10.00	0.27	0.557	179.29	0.555
	100.00	0.03	0.380	179.93	0.380
23.00	0.	22.10	1.128	165.17	0.929
	0.01	21.90	1.119	165.20	0.923
	0.05	21.75	1.096	165.24	0.915
	0.10	18.55	1.068	165.29	0.902
	0.20	11.02	1.008	166.50	0.887
	0.30	7.62	0.961	167.95	0.868
	0.40	5.80	0.925	169.28	0.852
	0.50	4.66	0.897	170.40	0.837
	1.00	2.30	0.809	173.88	0.779
	2.00	1.12	0.725	176.53	0.711
	5.00	0.43	0.625	178.51	0.620
	10.00	0.21	0.557	179.24	0.555
	100.00	0.02	0.380	179.92	0.380
28.75	0.	22.62	1.173	166.49	0.913
	0.01	22.50	1.162	166.69	0.910
	0.05	21.90	1.130	166.55	0.904
	0.10	16.38	1.095	166.66	0.889
	0.20	9.05	1.020	167.36	0.876
	0.30	6.19	0.969	168.54	0.859
	0.40	4.67	0.931	169.68	0.843
	0.50	3.73	0.902	170.67	0.829
	1.00	1.80	0.811	173.86	0.774
	2.00	0.86	0.726	176.43	0.709
	5.00	0.33	0.625	178.44	0.619
	10.00	0.16	0.557	179.20	0.555
	100.00	0.02	0.380	179.92	0.380
34.50	0.	23.08	1.225	167.18	0.902
	0.01	22.80	1.108	167.29	0.900
	0.05	22.28	1.167	167.81	0.892
	0.10	13.40	1.112	167.87	0.879
	0.20	7.29	1.030	168.34	0.866
	0.30	4.91	0.975	169.28	0.850
	0.40	3.67	0.936	170.24	0.835
	0.50	2.90	0.906	171.10	0.822
	1.00	1.37	0.813	173.97	0.770
	2.00	0.64	0.727	176.42	0.706
	5.00	0.24	0.625	178.41	0.618
	10.00	0.12	0.558	179.18	0.554
	100.00	0.11	0.380	179.91	0.380

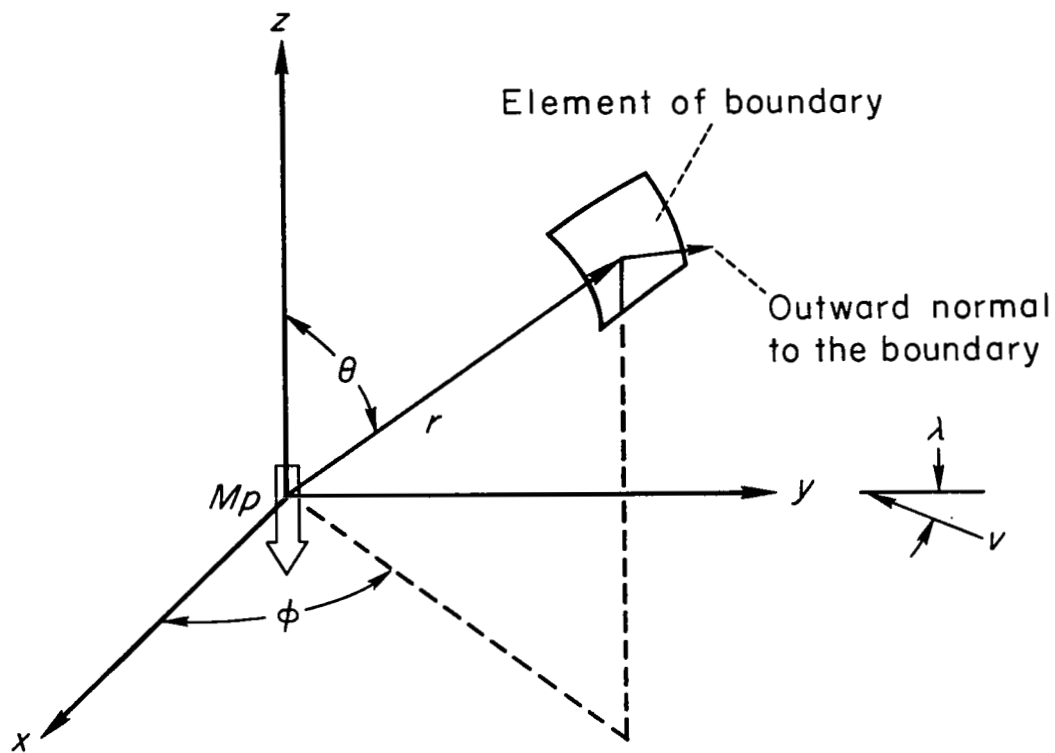


Figure 1.- View of coordinate system.

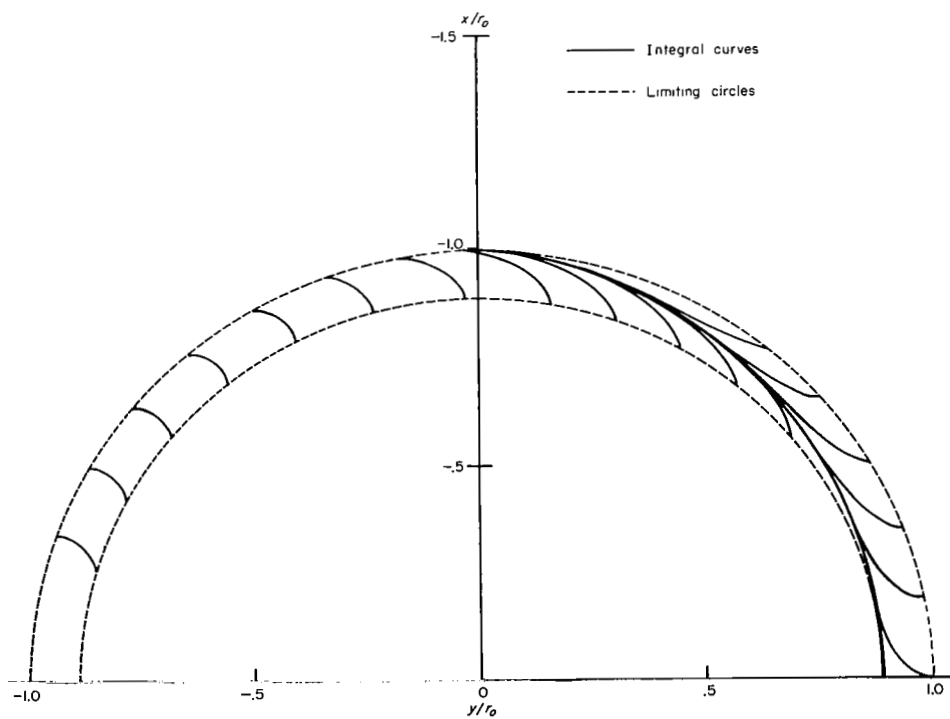


Figure 2.- Integral curves for equation (8) for $p_o/p_d = 1$.

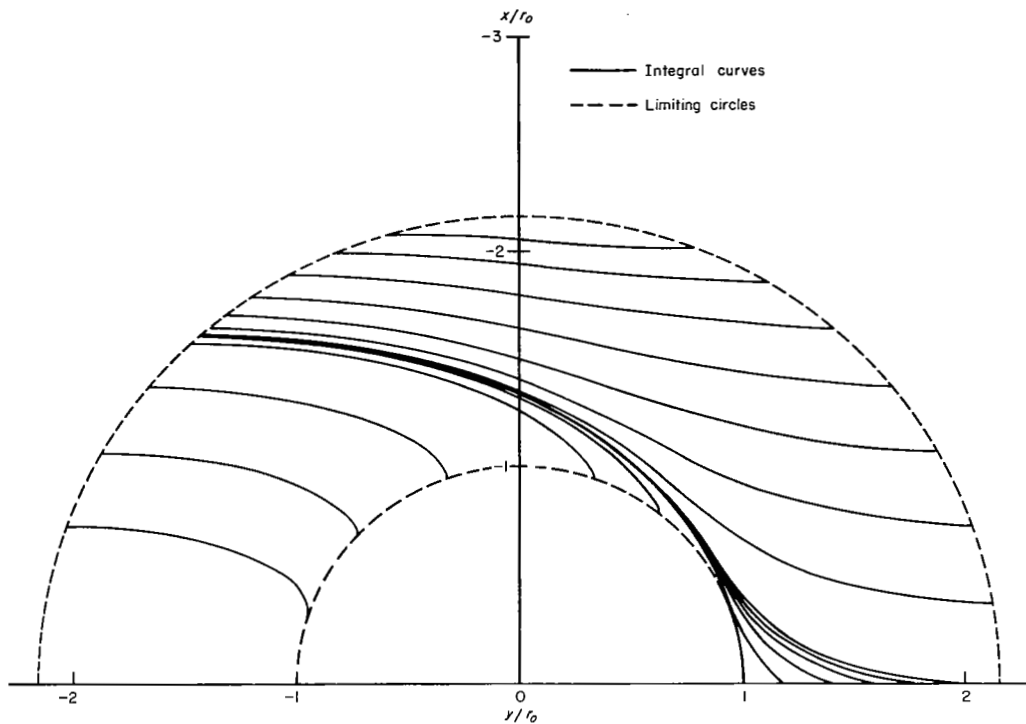


Figure 3.- Integral curves for equation (8) for $p_0/p_d = 0.01$.

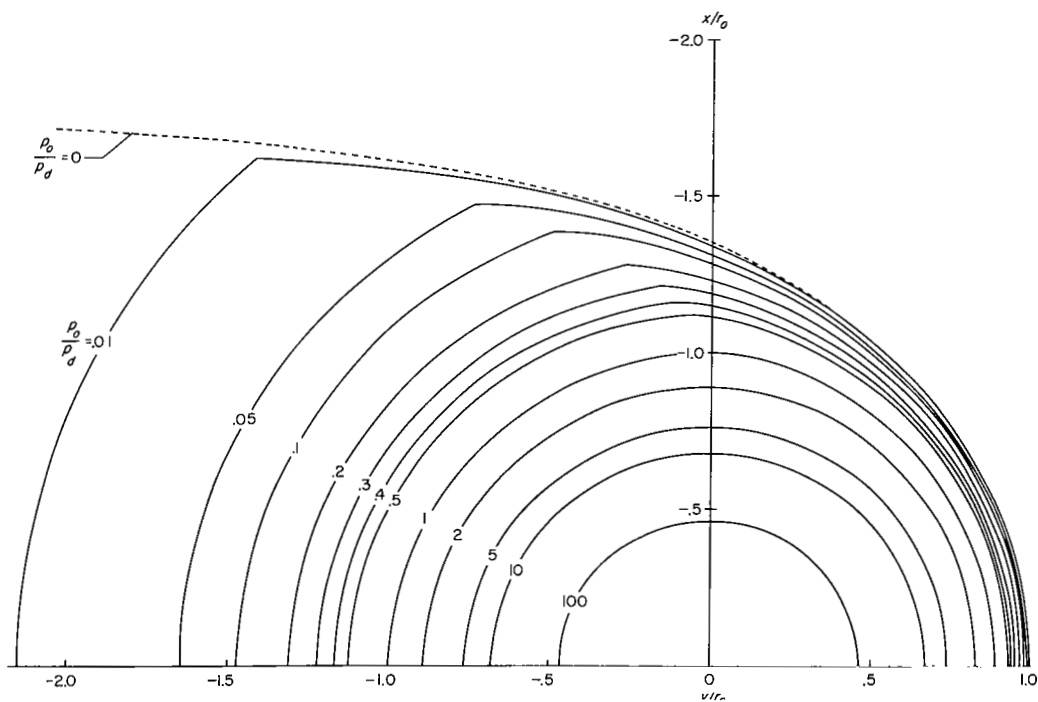
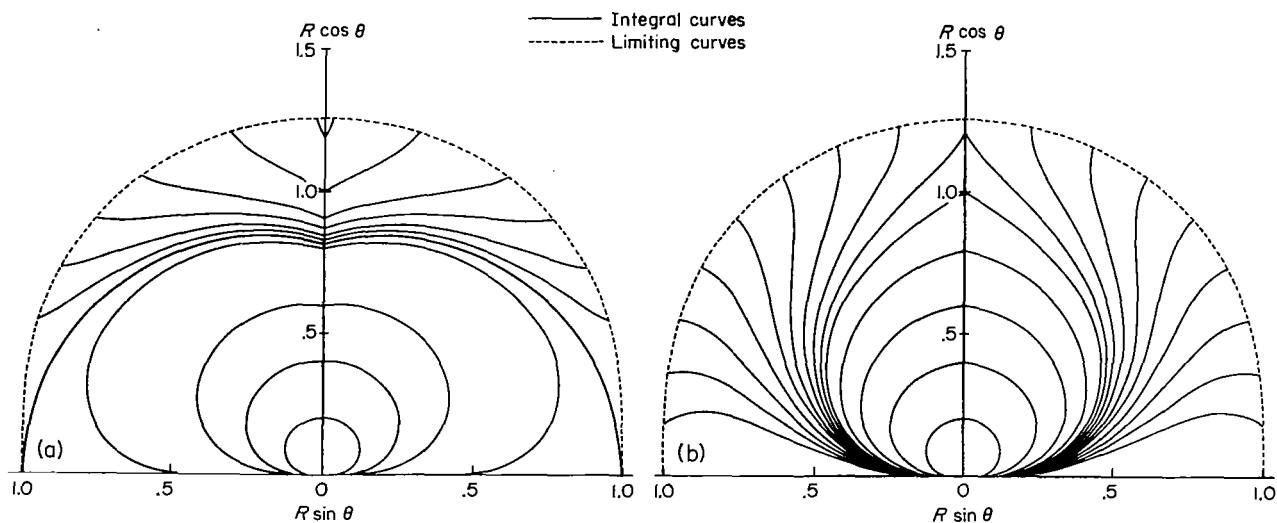


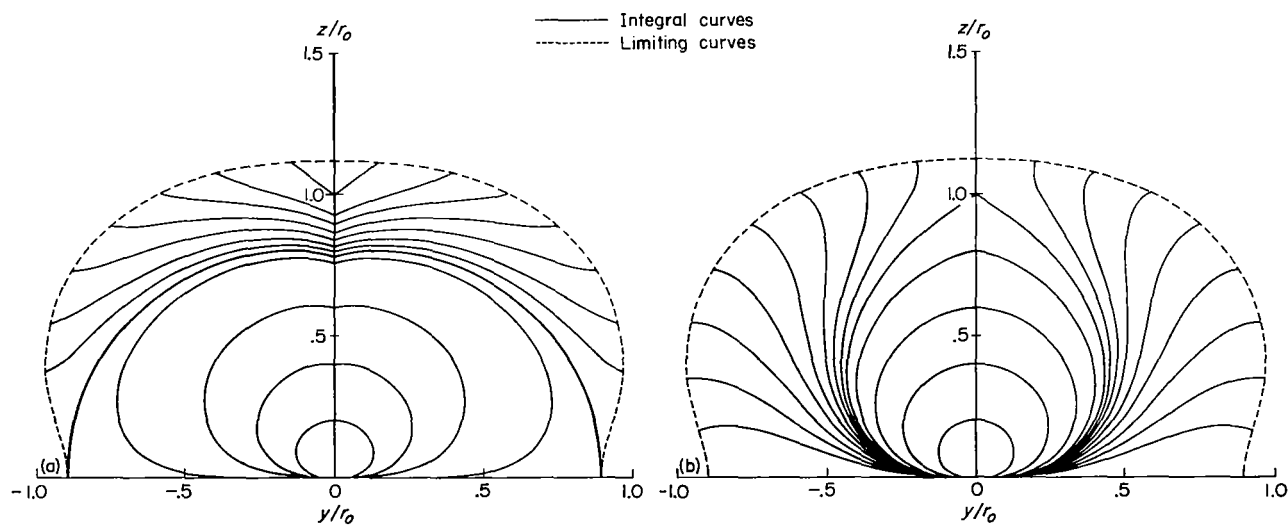
Figure 4.- Traces of the boundary of the geomagnetic field in the equatorial plane for various p_0/p_d , $\lambda = 0$.



(a) Upper sign.

(b) Lower sign.

Figure 5.- Integral curves for equation (14).



(a) Upper sign.

(b) Lower sign.

Figure 6.- Integral curves for equation (16) for $p_o/p_d = 1$.

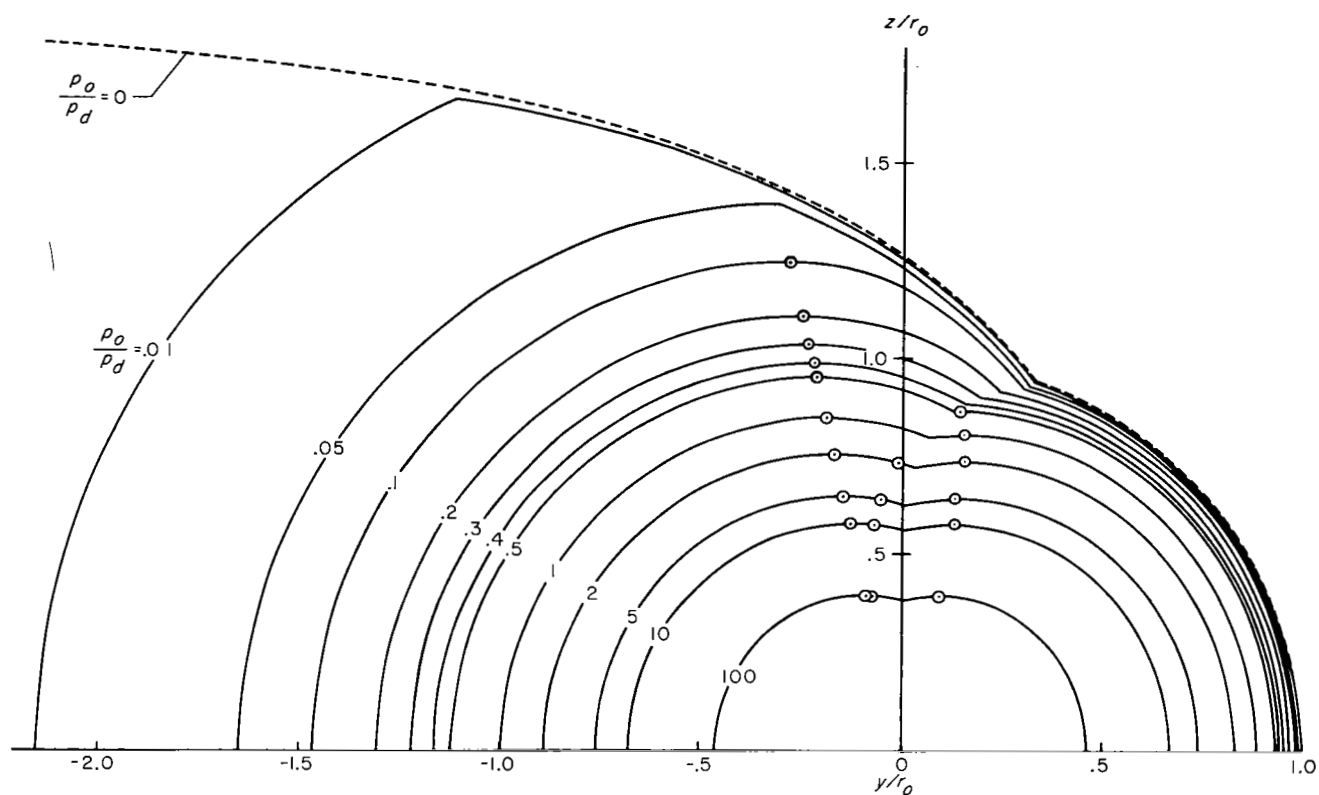


Figure 7.- Traces of the boundary of the geomagnetic field in the meridian plane containing the sun-earth line for various p_0/p_d , $\lambda = 0$.

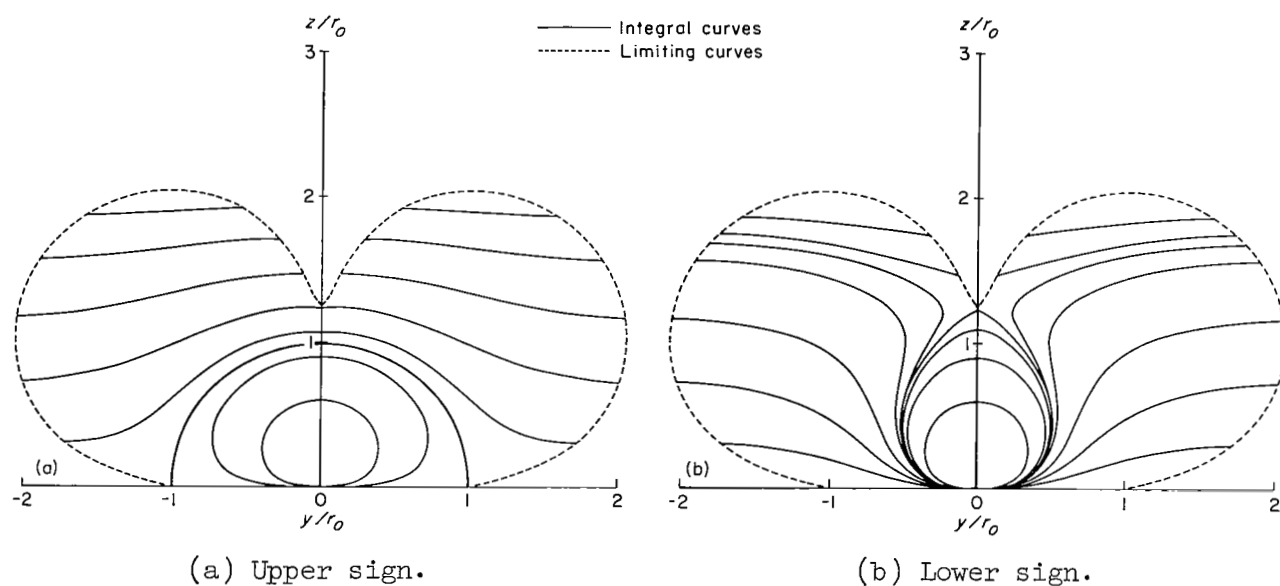


Figure 8.- Integral curves for equation (16) for $p_0/p_d = 0.01$.

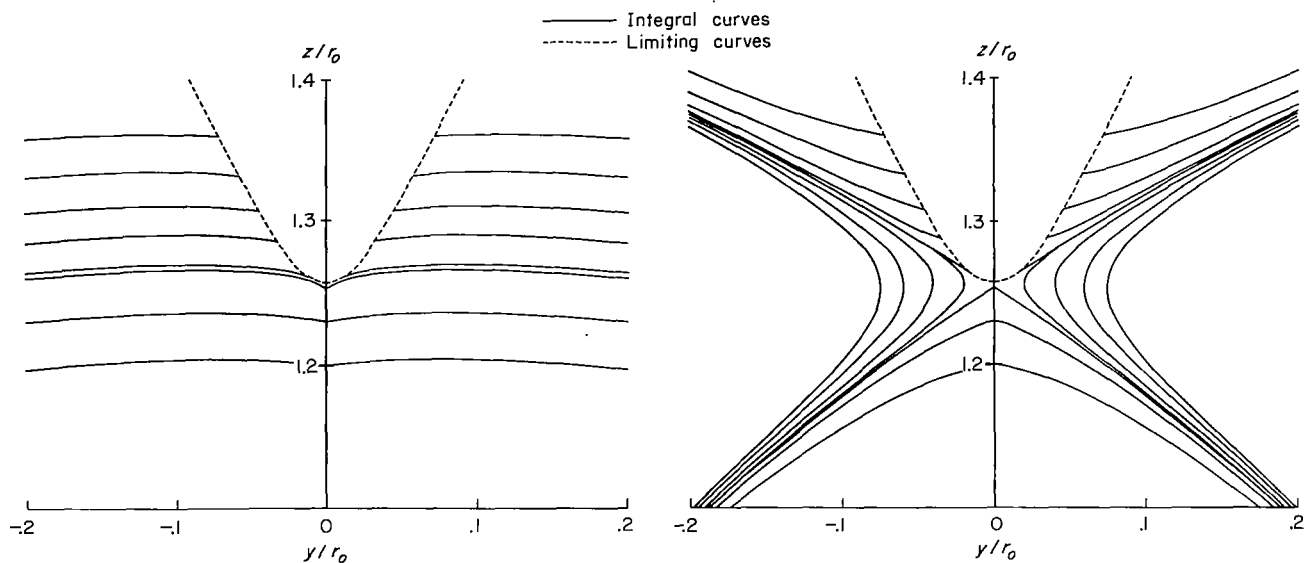


Figure 9.- Enlargements of plots of integral curves in the vicinity of the point of intersection of the polar axis and the limiting curve for $p_0/p_d = 0.01$, $\lambda = 0$.

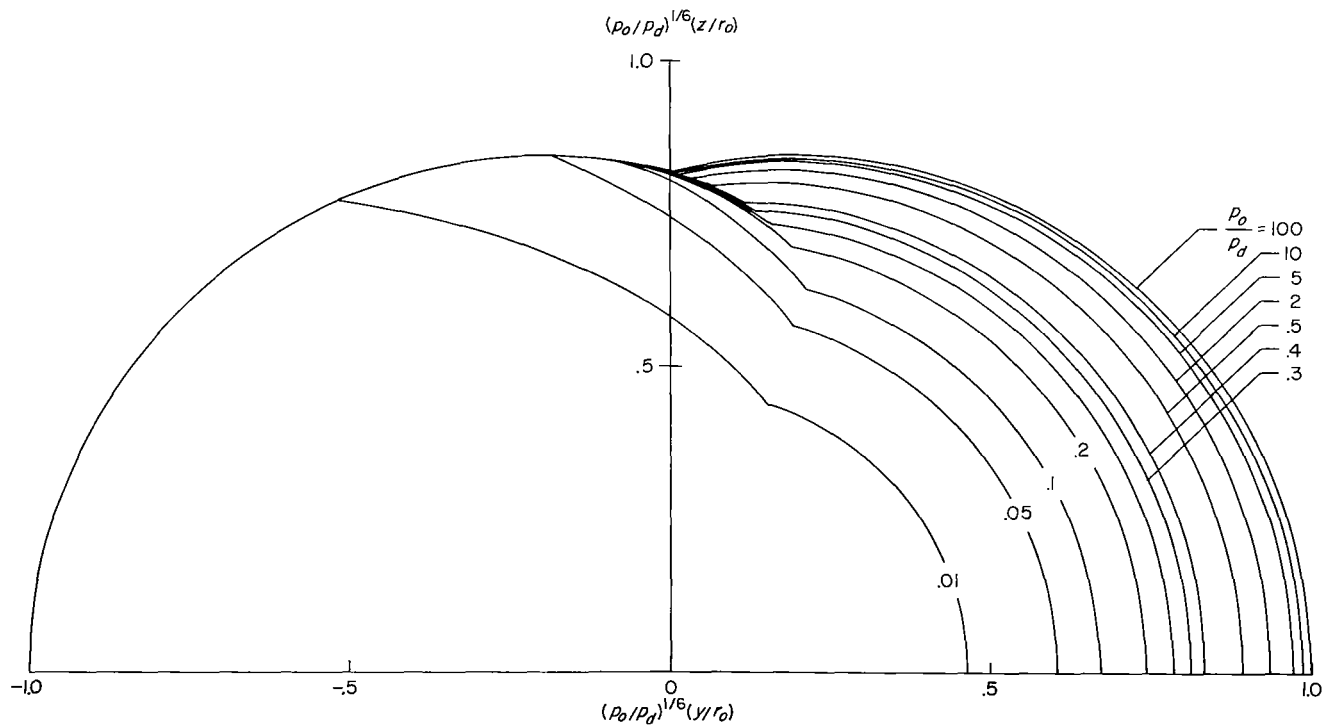


Figure 10.- Traces of the boundary of the geomagnetic field in the meridian plane containing the sun-earth line, plotted in terms of $\rho(p_0/p_d)^{1/6}$, for various p_0/p_d , $\lambda = 0$.

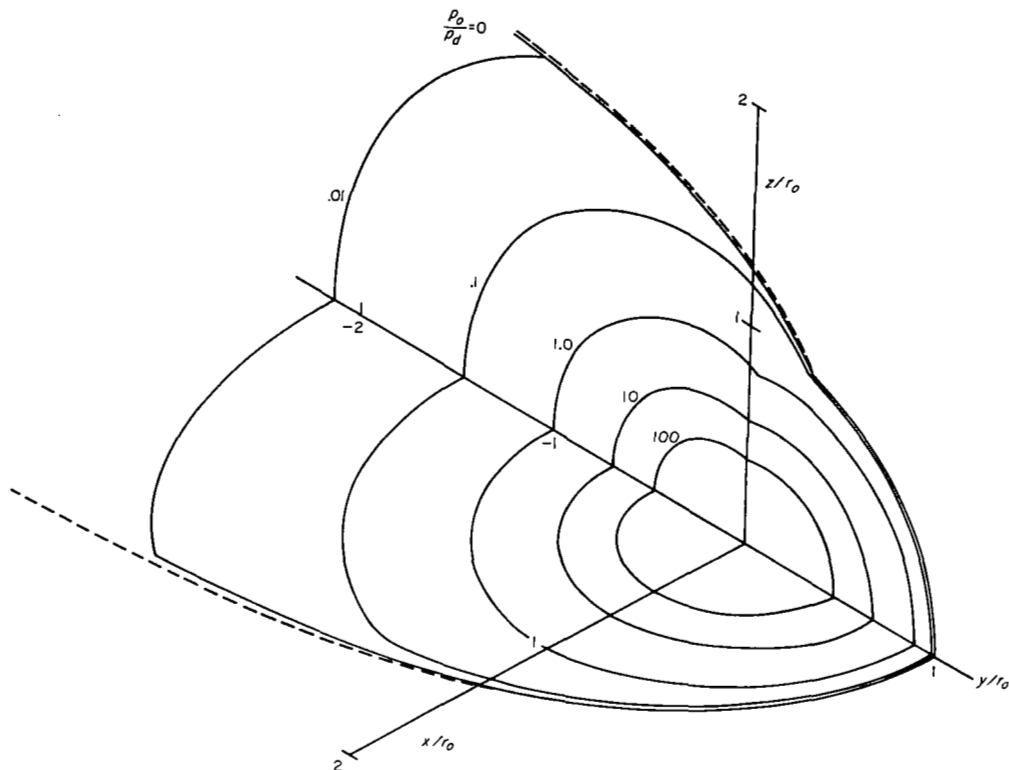


Figure 11.- Isometric drawing of the boundary of the geomagnetic field in the equatorial plane and the meridian plane containing the sun-earth line for various p_0/p_d , $\lambda = 0$.

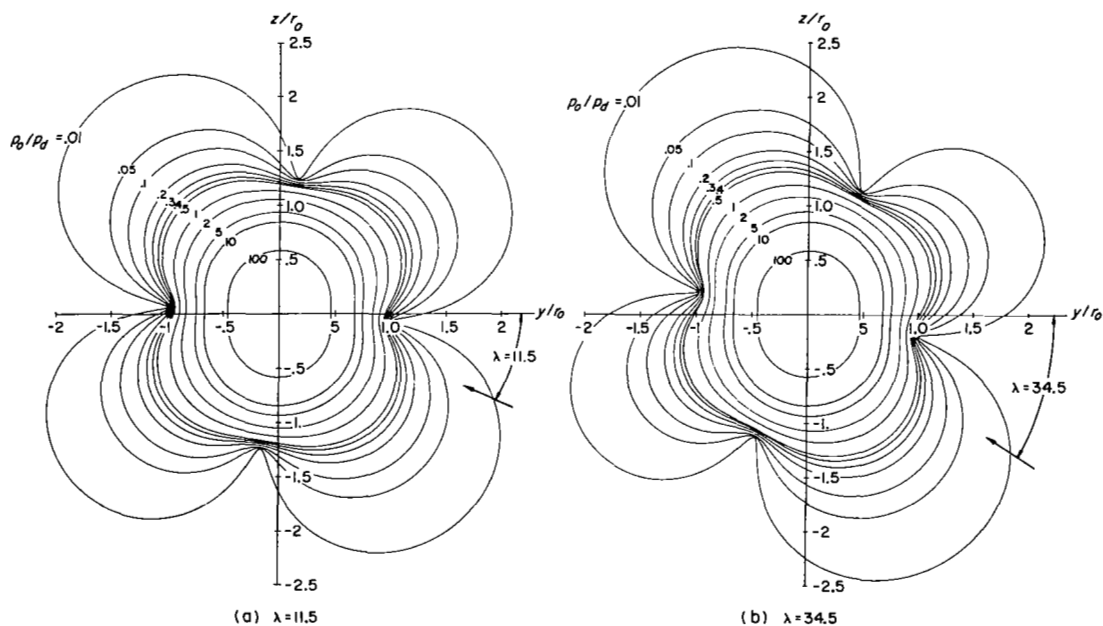


Figure 12.- Limiting lines defined by equation (23) for various p_0/p_d .

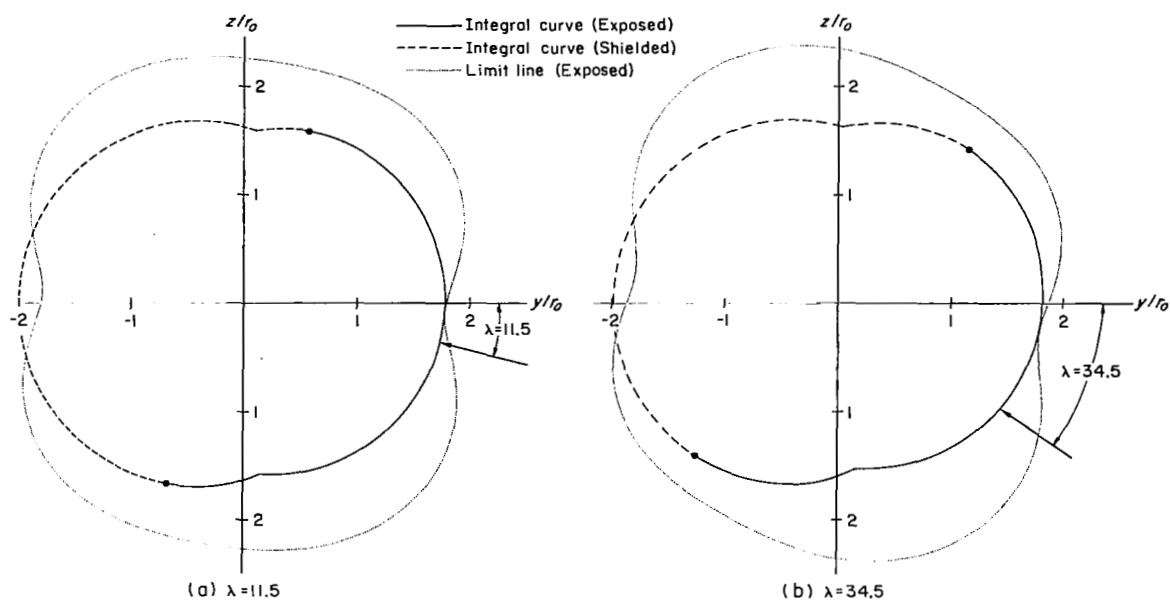


Figure 13.- Limiting lines and segments of integral curves required to represent the trace of the boundary of the geomagnetic field in the meridian plane containing the sun-earth line for $p_O/p_d = 1$.

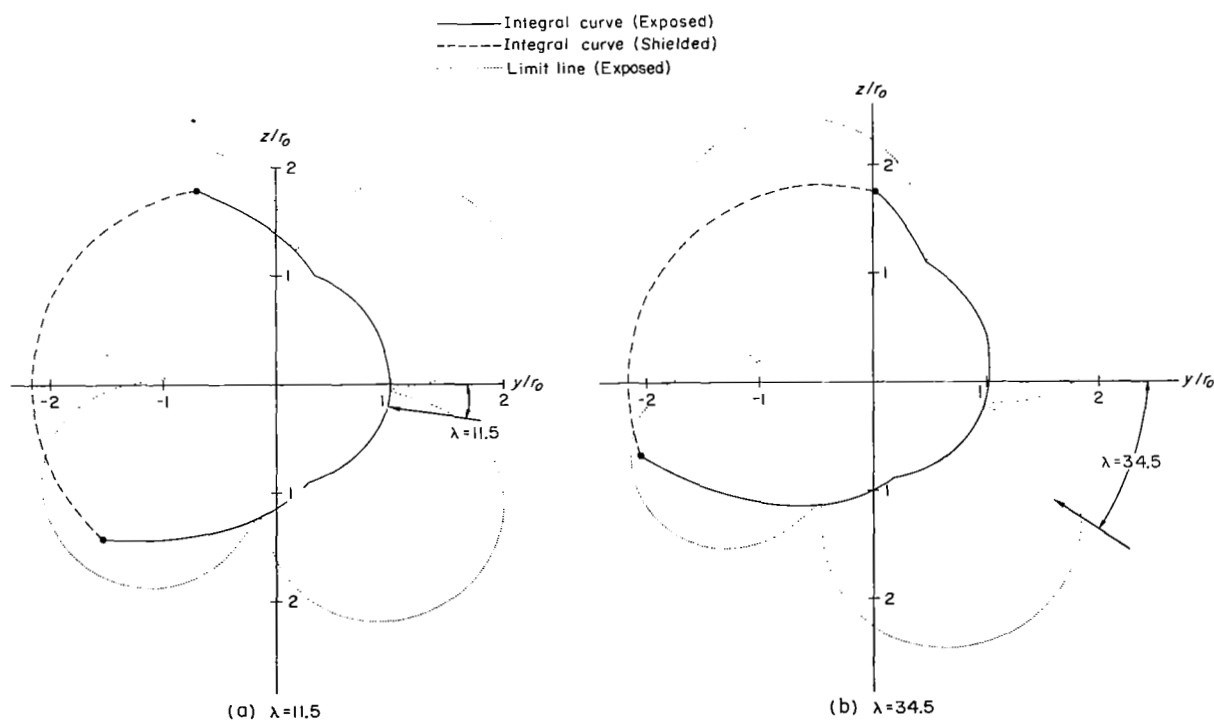


Figure 14.- Limiting lines and segments of integral curves required to represent the trace of the boundary of the geomagnetic field in the meridian plane containing the sun-earth line for $p_O/p_d = 0.01$.

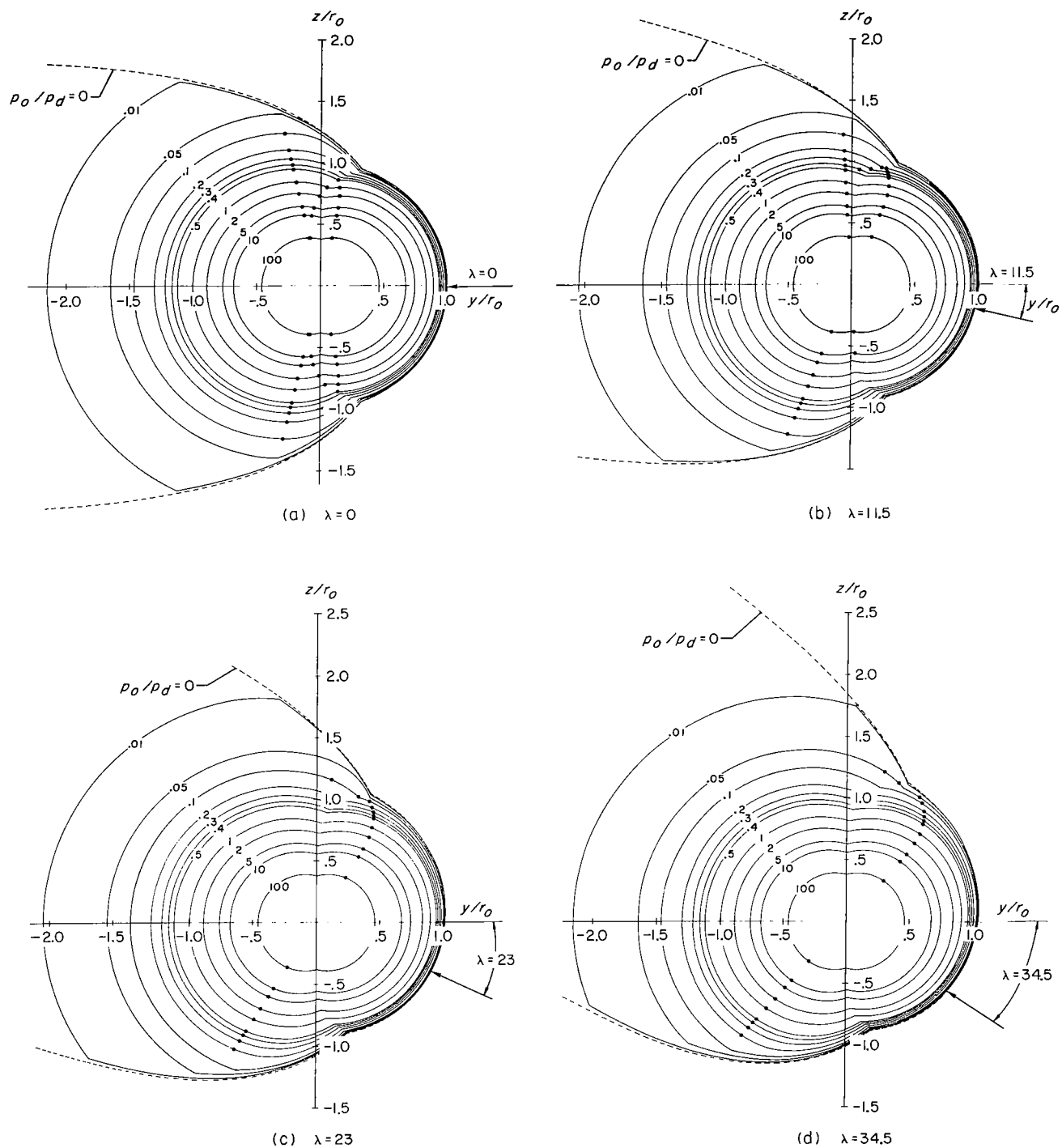


Figure 15.- Traces of the boundary of the geomagnetic field in the meridian plane containing the sun-earth line for various p_0/p_d and λ .